The Astrophysical Journal, 831:182 (20pp), 2016 November 10 doi:10.3847/0004-637X/831/2/182

THE GRISM LENS-AMPLIFIED SURVEY FROM SPACE (GLASS). VI. COMPARING THE MASS AND LIGHT IN MACS J0416.1-2403 USING FRONTIER FIELD IMAGING AND GLASS SPECTROSCOPY

A. Hoag[1], K.-H. Huang[1], T. Treu[2], M. Bradač[1], K. B. Schmidt[3], X. Wang[2,4], G. B. Brammer[5], A. Broussard[6], R. Amorin[7], M. Castellano[7], A. Fontana[7], E. Merlin[7], T. Schrabback[8], M. Trenti[9], and B. Vulcani[9]
[1] Department of Physics, University of California, Davis, CA 95616, USA
[2] Department of Physics and Astronomy, UCLA, Los Angeles, CA 90095-1547, USA
[3] Leibniz-Institut für Astrophysik Potsdam (AIP), An der Sternwarte 16, D-14482 Potsdam, Germany
[4] Department of Physics, University of California, Santa Barbara, CA 93106-9530, USA
[5] Space Telescope Science Institute, 3700 San Martin Drive, Baltimore, MD 21218, USA
[6] Department of Physics and Astronomy, Texas A&M, College Station, TX 77843, USA
[7] INAF—Osservatorio Astronomico di Roma, Via Frascati 33, 00040 Monte Porzio Catone, I-00040 Rome, Italy
[8] Argelander-Institut für Astronomie, Auf dem Hügel 71, D-53121 Bonn, Germany
[9] School of Physics, University of Melbourne, Parkville, Victoria, Australia
Received 2016 February 28; revised 2016 July 21; accepted 2016 July 29; published 2016 November 7

ABSTRACT

We present a model using both strong and weak gravitational lensing of the galaxy cluster MACS J0416.1-2403, constrained using spectroscopy from the Grism Lens-Amplified Survey from Space (GLASS) and Hubble Frontier Fields (HFF) imaging data. We search for emission lines in known multiply imaged sources in the GLASS spectra, obtaining secure spectroscopic redshifts of 30 multiple images belonging to 15 distinct source galaxies. The GLASS spectra provide the first spectroscopic measurements for five of the source galaxies. The weak lensing signal is acquired from 884 galaxies in the F606W HFF image. By combining the weak lensing constraints with 15 multiple image systems with spectroscopic redshifts and nine multiple image systems with photometric redshifts, we reconstruct the gravitational potential of the cluster on an adaptive grid. The resulting map of total mass density is compared with a map of stellar mass density obtained from the deep *Spitzer* Frontier Fields imaging data to study the relative distribution of stellar and total mass in the cluster. We find that the projected stellar mass to total mass ratio, $f_\star$, varies considerably with the stellar surface mass density. The mean projected stellar mass to total mass ratio is $\langle f_\star \rangle = 0.009 \pm 0.003$ (stat.), but with a systematic error as large as 0.004–0.005, dominated by the choice of the initial mass function. We find agreement with several recent measurements of $f_\star$ in massive cluster environments. The lensing maps of convergence, shear, and magnification are made available to the broader community in the standard HFF format.

Key words: galaxies: clusters: individual (MACS J0416.1-2403) – gravitational lensing: strong

Supporting material: figure set, machine-readable tables

1. INTRODUCTION

Gravitational lensing by galaxy clusters is now an important tool to probe astrophysics and cosmology (see Treu & Ellis 2014 for a recent review). The magnification of background objects produced by cluster lenses has been used to find extremely distant and faint galaxies (e.g., Zheng et al. 2012; Coe et al. 2013; Zitrin et al. 2014; Livermore et al. 2016). As a result, galaxy cluster fields are becoming increasingly popular for studying the epoch of reionization. Cluster-scale lensing has also been used to determine the spatial distribution of the total cluster mass, revealing insights into the physics of dark matter and structure formation (e.g., Bradač et al. 2006; Clowe et al. 2006; Sand et al. 2008; Newman et al. 2013; Sharon et al. 2014; Merten et al. 2015).

The Hubble Frontier Fields program (HFF; Lotz et al. 2016) is imaging six galaxy clusters and six parallel fields to extreme depths in seven optical and near-infrared (NIR) bands, using the Advanced Camera for Surveys (ACS) and the Wide Field Camera 3 (WFC3). A principal objective of the HFF initiative is to study magnified background objects, and accurate lens models are essential to determine their unlensed (intrinsic) properties. Lens models are primarily constrained by multiply imaged galaxies and weakly sheared sources. The added depth of the HFF images allows one to identify more multiply imaged galaxies, thus increasing the number of constraints and therefore the quality of the lens models. The CLASH[10] images (limiting magnitude ∼27 AB mag for a 5σ point source; Postman et al. 2012) revealed ∼10 candidate multiple image systems per cluster (Zitrin et al. 2015). The release of the HFF images (limiting magnitude ∼29 AB mag for a 5σ point source) has approximately tripled the number of known multiply imaged galaxies for the four clusters analyzed so far (e.g., Jauzac et al. 2014, 2015b; Diego et al. 2015b; Wang et al. 2015; Treu et al. 2016).

While the imaging data of the HFF have enabled the photometric identification of a large number of multiply imaged systems, the redshifts of many systems remain uncertain without spectroscopic follow-up. The redshifts must be well constrained in order to be useful for the lens models. It has recently been shown that the number of *spectroscopic* systems has a strong influence on the quality of the lens model (Rodney et al. 2015a, 2015b). Photometric redshifts are useful when spectroscopy is lacking, but they can be prone to catastrophic errors, especially for sources at or near the limiting magnitude of the image. An alternative approach to photometric redshifts is to estimate the redshift of new multiply

[10] The Cluster Lensing and Supernova Survey with Hubble (CLASH); http://www.stsci.edu/~postman/CLASH/Home.html.

imaged systems using an existing model (e.g., Jauzac et al. 2014). This method can potentially introduce confirmation bias in the modeling process. That is, unless a correct lens model has already been obtained, the predicted redshifts of the multiply imaged galaxies may be incorrect, and the uncertainties may be underestimated. Unless decided upon in advance, different approaches to determining redshifts in the absence of spectroscopic data can lead to different constraints among teams modeling the same cluster.

It is therefore paramount to obtain spectroscopic redshifts for the multiply imaged systems in the HFF. The Grism Lens-Amplified Survey from Space (GLASS) is one such effort. GLASS[11,12] is a large *Hubble Space Telescope* (*HST*) program that has surveyed 10 galaxy cluster fields with WFC3/IR grisms, including all six HFF clusters. For details on the observation strategy and data products of GLASS, see Schmidt et al. (2014) and Treu et al. (2015).

In this paper, we present new spectroscopic redshifts from GLASS data for MACS J0416.1-2403 (MACS J0416 hereafter) and combine them with redshifts from the literature to model the total mass distribution of MACS J0416. When spectroscopy is not available, we use photometric redshifts obtained by the ASTRODEEP team (Castellano et al. 2016; Merlin et al. 2016), which we test against GLASS spectra of singly imaged objects. We also determine the stellar mass to total mass ratio of the cluster using *Spitzer*/Infrared Array Camera (IRAC) data to infer the cluster stellar mass distribution. The paper is organized as follows. In Section 2 we give an overview of the optical and NIR HFF and mid-IR *Spitzer* Frontier Fields imaging data, as well as the GLASS NIR spectroscopic data. In Section 3 we briefly cover the reduction and analysis of the GLASS data. In Section 4 we describe the process of selecting the set of multiple images used to constrain the lens model and discuss the GLASS spectroscopic measurements. In Section 5 we present our lens model and compare it with other lens models of the cluster using similar constraints. In Section 6, we study the relative distribution of stellar and total mass. Finally, we summarize our results in Section 7. We adopt a standard concordance cosmology with $\Omega_m = 0.3$, $\Omega_\Lambda = 0.7$, and $h = 0.7$. All magnitudes are given in the AB system (Oke 1974).

2. IMAGING AND GROUND-BASED SPECTROSCOPIC DATA

Discovered by the Massive Cluster Survey (MACS; Ebeling et al. 2001) as a result of its large X-ray luminosity ($\sim 10^{46}$ erg s^{-1}, Mann & Ebeling 2012), MACS J0416 was found to likely be a binary head-on merging cluster system. The first optical and NIR *HST* imaging data of MACS J0416 were obtained by the CLASH survey. The ESO VIMOS large program CLASH-VLT (186.A-0798; PI: P. Rosati), a spectroscopic campaign designed to obtain thousands of optical spectra in the CLASH cluster fields with VIMOS on the Very Large Telescope (VLT), recently found further evidence for the merging state of the cluster (Balestra et al. 2016).

In this work, we construct our lens model using the deepest optical and NIR imaging and spectroscopy data newly acquired with *Hubble*, as part of the HFF initiative (Section 2.1) and the GLASS program (Section 3), following our study of Abell 2744 in Wang et al. (2015). We make use of the most current spectroscopic catalog from CLASH-VLT (Balestra et al. 2016) to help constrain the lens model. We also use mid-IR imaging data acquired with the IRAC on board the *Spitzer Space Telescope* (Section 2.2; Fazio et al. 2004; Werner et al. 2004) obtained by the DDT program #90258 (PI: Soifer; P. Capak et al. 2016, in preparation) and #80168 (PI: Bouwens) to infer the stellar mass distribution of cluster members.

2.1. HFF Imaging

Ultradeep *HST* images of six clusters (Abell 370, Abell 2744, RX J2248, MACS J0416, MACS J0717, and MACS J1149) are being obtained as part of the HFF.[13] The 5σ point-source limiting magnitudes are roughly 29 mag in both the ACS/optical filters (F435W, F606W, F814W) and WFC3/IR filters (F105W, F125W, F140W, F160W). The observations were divided into two epochs in order to obtain the same depth in ACS and WFC3/IR for the primary and parallel fields. All observations of MACS J0416 were completed in 2014 September. In this work, we use the mosaics drizzled onto a $0\farcs06$ pix^{-1} grid.

2.2. Spitzer Frontier Fields

As a part of the HFF campaign, deep *Spitzer*/IRAC images in channels 1 and 2 (at 3.6 μm and 4.5 μm, respectively) were taken through the *Spitzer* Frontier Fields program.[14] In this work, we use the full-depth *Spitzer*/IRAC mosaics for MACS 0416 released by P. Capak et al. (2016, in preparation). The IRAC mosaics reaches ~50 hr depth per channel in the HFF *primary* field and the *parallel* field (~6′ to the west of the primary field). Due to constraints on *Spitzer*'s roll angle and low-background requirements, six additional *flanking* fields exist around the HFF primary and parallel fields with uneven coverage in channels 1 and 2. The exposures were drizzled onto a $0\farcs6$ pix^{-1} grid, and within the footprint of the *HST* primary field there are ~1800 frames (with `FRAMETIME` ~ 100 s) per output pixel. In the primary and parallel fields, the nominal 5σ depth of a point source reaches 26.6 mag at 3.6 μm and 26.0 mag at 4.5 μm. However, this sensitivity might not be reached near the cluster center due to blending with cluster members and the diffuse intracluster light (ICL).

3. GLASS OBSERVATIONS AND DATA REDUCTION

GLASS (GO-13459; PI: Treu; Schmidt et al. 2014; Treu et al. 2015) observed 10 massive galaxy clusters with the *HST* WFC3-IR G102 and G141 grism between 2013 December and 2015 January. Each of the clusters targeted by GLASS has deep multi-band *HST* imaging from the HFF (Section 2.1) and/or from CLASH. Each cluster is observed at two position angles (P.A.s) approximately 90° apart to facilitate deblending and extraction of the spectra. Short exposures are taken through filters F105W or F140W during every visit to help calibrate the spectra, model the background, model the contaminating objects, and identify supernovae by difference imaging. The total exposure time per cluster is 14 orbits, distributed so as to provide approximately uniform sensitivity across the entire wavelength coverage of 0.8–1.7 μm. Parallel observations are taken with the ACS F814W direct image and G800L grism to

[11] http://glass.astro.ucla.edu
[12] http://dx.doi.org/10.17909/T9KG60
[13] http://dx.doi.org/10.17909/T9KK5N
[14] http://ssc.spitzer.caltech.edu/warmmission/scheduling/approvedprograms/ddt/frontier/

Table 1
GLASS Grism and Imaging Exposure Times for MACS J0416

Filter	P.A. (deg.)	$t_{exp.}$ (s)
G102	164	10929
G102	247	10929
G141	164	4312
G141	247	4312
F105W	164	1068
F105W	247	1068
F140W	164	1573
F140W	247	1423

Note. Exposure times are for the cluster core of MACS J0416 only.

map the cluster infall regions. Here we focus on the NIR data on the cluster core of MACS J0416.

The two P.A.s of GLASS data analyzed here were taken on 2014 November 23 and 30 (P.A. = 164°) and 2015 January 13 and 18 (P.A. = 247°). The resulting total exposure times for the individual grism observations are shown in Table 1. Prior to reducing the complete GLASS data, He Earth-glow is removed from individual exposures (Brammer et al. 2014).

In Figure 1 we show a color composite image of MACS J0416, using the optical and NIR coadded imaging from HFF and CLASH combined with the NIR imaging from GLASS. The green (red) square shows the GLASS footprint for P.A. = 164° (P.A. = 247°). The fiducial cluster redshift used by the HFF lens modeling team and adopted throughout the paper is $z_{\rm cluster} = 0.396$. The two brightest cluster galaxies (BCGs) (NE and SW) are labeled in the figure. The NE BCG and the SW BCG are at redshifts $z = 0.395$ and $z = 0.400$, respectively (Balestra et al. 2016).

The GLASS observations are designed to follow the 3D-*HST* observing strategy (Brammer et al. 2012) and were processed with an updated version of the 3D-*HST* reduction pipeline[15] (Momcheva et al. 2015). Below we summarize the main steps in the reduction process of the GLASS data but refer to Brammer et al. (2012), Momcheva et al. (2015), and the GLASS survey paper (Treu et al. 2015) for further details. The GLASS data were taken in a four-point dither pattern identical to the one shown in Figure 3 of Brammer et al. (2012) to reduce susceptibility to bad pixels and cosmic rays and to improve sub-pixel sampling of the WFC3 point-spread function. At each dither position, a direct and a grism exposure were taken. The direct images are commonly taken in the filter with passband overlapping in wavelength with the grism, i.e., F105W for G102 and F140W for G141. However, to accommodate searches for supernovae and the characterization of their light curves in GLASS clusters, each individual visit is designed to have imaging in both filters. Hence several pairs of F140W +G102 observations exist in the GLASS data. This does not affect the reduction or the extraction of the individual GLASS spectra.

The individual exposures were combined into mosaics using AstroDrizzle from the DrizzlePac software package (Gonzaga 2012). All direct image exposures were aligned using `tweakreg`, with background subtracted from the exposures by fitting a second-order polynomial to each of the source-subtracted exposures. We subtracted the background of the grism exposures using the master sky images and algorithm presented by Brammer et al. (2015). The individual sky-subtracted exposures were combined using a pixel scale of 0.″06 per pixel (about half a native WFC3 pixel). Figure 2 shows the full field-of-view mosaics of the two NIR grisms (G102 on the left and G141 on the right) at the two GLASS position angles for MACS J0416. The contamination model was computed and one- and two-dimensional spectra were extracted from 2×2 "interlaced" versions of the grism mosaics following the procedure outlined in detail by Momcheva et al. (2015), where the source positions and extent were determined with the `SExtractor` (Bertin & Arnouts 1996) software run on the corresponding direct image mosaics. The extraction of grism spectra used in this work is based on a public HFF photometric catalog available on the STScI MAST archive,[16] supplemented by our own photometric catalogs based on CLASH images and GLASS direct images.

4. IDENTIFICATION OF MULTIPLE IMAGES

In this section we describe how we identify and vet multiple image candidates using the HFF imaging data (Section 4.1) and GLASS spectroscopic data (Sections 4.2 and 4.3).

4.1. Imaging Data: Identification and Photometric Redshifts

Zitrin et al. (2013) published the first detailed strong lensing analysis of MACS J0416. They identified over 70 multiple images (23 source galaxies) in the CLASH imaging data, making MACS J0416 the most prolific CLASH cluster in terms of multiply imaged galaxies (Zitrin et al. 2015). With the addition of the much deeper HFF data, 272 multiple images (92 source galaxies) have been identified behind MACS J0416 (Jauzac et al. 2014; Diego et al. 2015a). We list all the multiple images in Table 2 and show their positions behind the cluster in Figure 3.

Several efforts have been made to spectroscopically confirm the redshifts of the strongly lensed galaxy candidates in MACS J0416 (Zitrin et al. 2013; Jauzac et al. 2014; Richard et al. 2014; Balestra et al. 2016; Grillo et al. 2015; S. Rodney et al. 2016, in preparation). Images belonging to systems 1, 2, 3, 4, 5, 7, 10, 13, 14, 16, 17, 23, 26, and 28 have been targeted by multiple authors, leading to agreement in the spectroscopic redshift within the uncertainties, with the exception of system 14. This system will be discussed in more detail in Section 4.2. When spectroscopy is unavailable, confirming images that belong to the same source is more difficult.

Inspired by a previous collaborative effort to model the HFF clusters as well as the recent rigorous vetting procedure developed by Wang et al. (2015), a new collaborative effort was undertaken by seven teams simultaneously modeling the HFF galaxy clusters to assign quality grades to the multiple image candidates. The grading was done independently by each of the seven teams and focused on ensuring consistency of the morphologies and colors of multiple images of the same source galaxy. Each team assigned each multiple image candidate a grade on a scale from 1 to 4, where 1 meant secure and 4 meant untrustworthy. The results from the grading process were divided into the categories: "Gold," "Silver," and "Bronze." The Gold category was reserved for spectroscopically confirmed multiple images that also received an average grade of <1.5. The multiple images confirmed using GLASS

[15] http://code.google.com/p/threedhst/

[16] http://dx.doi.org/10.17909/T9KK5N

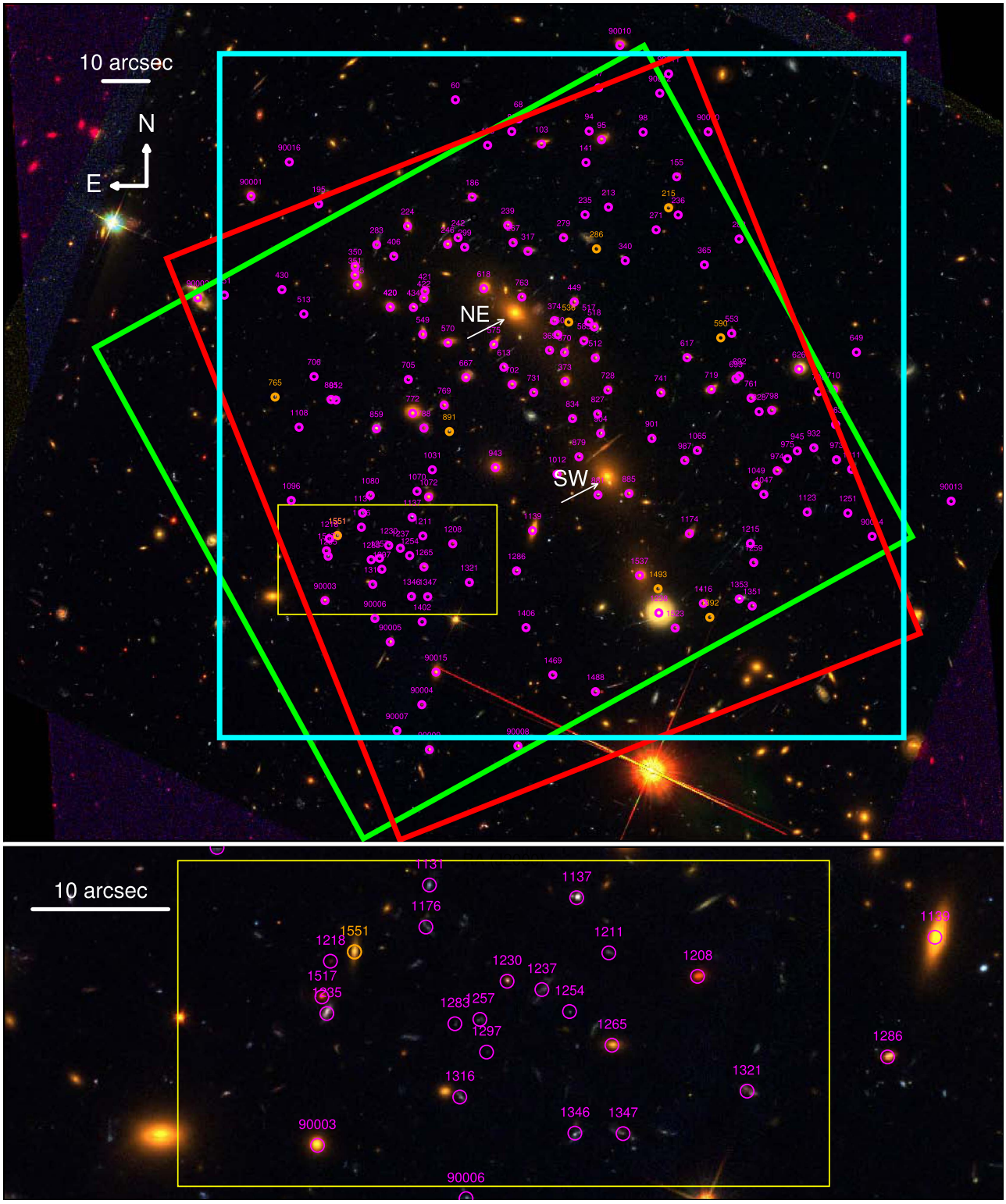

Figure 1. Top panel: all objects that we confirm spectroscopically with GLASS in MACS 0416. The color coding of the circles reflects the quality of the GLASS spectroscopic redshift (see "Quality" in Table 3: 3 = orange, 4 = magenta). The labels on the circles are the GLASS IDs. The two distinct P.A.s of the spectroscopic GLASS pointings are shown by the green (P.A. = 164°) and red (P.A. = 247°) squares. There are a few objects that fall outside the direct image field of view (FOV). Their spectra were dispersed onto the chip, so they could still be extracted and analyzed (see Figure 2). The cyan square outlines the area shown in Figure 3. The yellow rectangle shows the zoomed-in region also displayed in the bottom panel. The white arrows point to the two BCGs (NE and SW), which are separated by $\Delta V_{\rm r.f.} \sim 900$ km s^{-1} (Balestra et al. 2016) and are likely in a merging state (Mann & Ebeling 2012; Jauzac et al. 2015a; Ogrean et al. 2015). Bottom panel: a zoomed-in portion of the field shown in the top panel where the density of confirmed objects is highest. The yellow rectangle is the same one shown in the top panel. In both panels, the color composite image of MACS J0416 is composed of the F435W, F606W, and F814W images from HFF (Lotz et al. 2016) and CLASH (Postman et al. 2012).

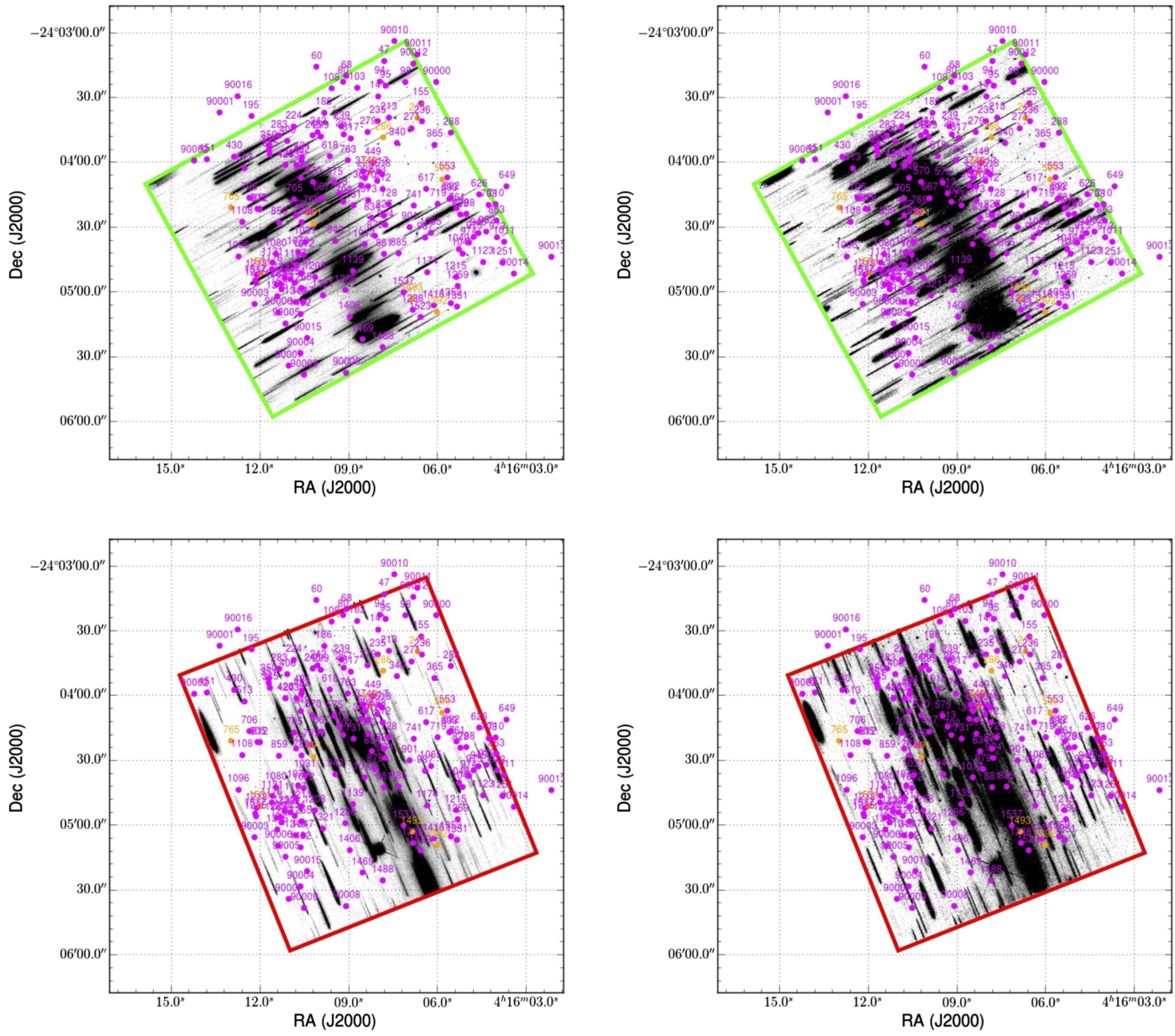

Figure 2. The GLASS G102 (left) and G141 (right) grism pointings of MACS J0416 at two distinct P.A.s, with FOV shown by the green (P.A. = 164°) and red (P.A. = 247°) squares. The circles in all panels denote the positions of the emission line objects identified in this work (Table 3), with color coding and labels following the conventions adopted in Figure 1. The circles that fall outside the grism pointings are identified in *HST* images with a larger FOV than the individual grism FOVs. These objects can still be observed in the grism data because their first-order spectra are dispersed onto the chip.

spectroscopy that are presented in this work were included in the Gold sample. The Silver category corresponded to images lacking spectra but receiving a unanimous vote of 1. Bronze was assigned to images lacking spectra and receiving an average grade of >1 but <1.5. Images lacking spectra and receiving an average grade of ≥ 1.5 were not used by the modeling teams.

For our lens model, we decided to consider only multiple images in the Gold and Silver categories, which included 80/31 total multiple images/systems. In order to use a Silver multiple image in the lens model, it was necessary to estimate its redshift. Because the grading was done via visual inspection, it was not guaranteed that every multiple image would be detected in our photometric catalog. Of the 31 systems comprising Gold and/or Silver images, only 26 were included in our lens model. Five systems (systems 8, 33, 40, 41, and 51, all are graded Silver) are not included in our model because of problems with photometry and redshift. Neither of the two Silver images in system 8 was detected in the photometric catalog, most likely due to their faintness and proximity to bright cluster members. Systems 33, 40, and 51 had poorly constrained probability density functions (PDFs) for photometric redshift. Only a single image in system 41 was detected in the photometric catalog, and its redshift was too poorly constrained to use in the lens model. The redshift PDFs for the multiple images in systems 33, 40, 41, and 51 are shown in Appendix A.

For the remaining Silver images, it was necessary to compute photometric redshifts to include them in the lens model. For these systems we used photometric redshifts

Table 2
Multiply "Imaged" Arc Systems Identified in the MACS J0416 Field

ID_{arc}	ID_{GLASS}	R.A. (deg.)	Decl. (deg.)	Cref.	$z_{spec}(1)$	$z_{ref}(1)$	$z_{spec}(2)$	$z_{ref}(2)$	z_{grism}	z_{Bayes}	F140W (mag.)	Magnification[a]	Sample
1.1	245	64.040750	−24.061592	MJ14	1.896	LC12	1.89	MJ14	…	$1.9^{+0.1}_{-0.1}$	23.92 ± 0.02	$5.40^{+0.48}_{-0.10}$	Gold
1.2	244	64.043479	−24.063542	MJ14	1.896	MJ14	1.896	JR14	…	…	23.43 ± 0.02	$51.02^{+236.36}_{+28.13}$	Gold
1.3	571	64.047354	−24.068669	MJ14	1.896	MJ14	1.896	JR14	…	…	25.09 ± 0.03	$4.03^{+0.12}_{-0.04}$	Gold
2.1	268	64.041183	−24.061881	MJ14	1.8925	MJ14	1.8925	JR14	1.90	$2.4^{+0.1}_{-0.2}$	23.01 ± 0.01	$8.26^{+0.97}_{-0.61}$	Gold
2.2	248	64.043004	−24.063036	MJ14	1.8925	MJ14	1.8925	JR14	1.89	…	23.08 ± 0.01	$8.49^{+0.34}_{-0.70}$	Gold
2.3	572	64.047475	−24.068850	MJ14	1.8925	MJ14	1.8925	JR14	1.90	…	22.97 ± 0.01	$4.13^{+0.29}_{-0.37}$	Gold
3.1	494	64.030783	−24.067117	MJ14	1.9885	MJ14	1.9885	JR14	1.99	$2.5^{+0.1}_{-0.3}$	23.32 ± 0.01	$4.13^{+0.03}_{-0.09}$	Gold
3.2	372	64.035254	−24.070981	MJ14	1.9885	MJ14	1.9885	JR14	1.99	…	23.13 ± 0.01	$2.27^{-0.02}_{-0.06}$	Gold
3.3	…	64.041817	−24.075711	MJ14	1.9885	MJ14	1.9885	JR14	1.99	…	…	$3.20^{+0.12}_{-0.01}$	Gold

Notes. ID_{arc} numbers for multiple image systems 19–22 are intentionally omitted for consistency with IDs from the recent literature (e.g., Jauzac et al. 2014). Entries where ID_{arc} ends in "p" refer to proposed multiple candidates, which are less confident identifications. Entries where ID_{arc} ends in "a" offer alternative images to those with the same ID listed without "a." Entries where ID_{GLASS} is listed as "..." had no match in the grism detection image. R.A. and decl. reference the HFF v1.0 60 mas mosaics. Cref. lists the short names for publications in which the coordinates have appeared or will appear, if publication is in preparation. Some multiple images have been targeted with spectroscopy by multiple authors. We list at most two references to spectroscopic redshifts, reporting the number of significant figures as they appear in each reference (LC12 = Christensen et al. (2012), MJ14 = Jauzac et al. (2014), TJ14 = Johnson et al. (2014), SR14 = S. Rodney et al. (2016, in preparation), JPK = J.-P. Kneib et al. (2016, in preparation), D15 = Diego et al. (2015a), RK = R. Kawamata et al. (2016, in preparation), JR14 = Richard et al. (2014), AZ13 = Zitrin et al. (2013), CG15 = Grillo et al. (2015), IB15 = Balestra et al. (2016), GC16 = Caminha et al. (2016)). z_{grism} is the grism redshift we measure in this work. The typical uncertainty on z_{grism} is 0.01, corresponding to a grism wavelength uncertainty of ∼50 Å. z_{Bayes} is the redshift obtained for a mulitple image system from hierarchical Bayesian modeling. z_{Bayes} (95% confidence limits) is shown only for systems with two or more reliable measurements of photometric redshift. Objects for which F140W magnitudes (68% confidence limits) are listed as "..." are not detected in our photometric catalog. The magnification (68% confidence limits) was calculated using the best-fit lens model scaled to the spectroscopic redshift of the mulitple image system, or z_{Bayes} if the spectroscopic redshift was not known. The "Sample" column refers to the category in which the HFF lens modeling assigned each multiple image based on the spectroscopic and photometric constraints. Only Gold and Silver images were used to constrain our lens model.

[a] Some multiple images have best-fit magnifications that are outside the 68% confidence interval due to non-Gaussian error distributions.

[b] Systems 3 and 4 are believed to be different subtructures of the same source galaxy due to the similar redshift and spatial position of the multiple images in each system.

[c] The GLASS spectroscopic redshifts of 5.1 and 5.4 were determined after the HFF modeling procedure took place. Therefore, neither image was included in the Gold sample.

[d] 12.3 does not belong to the Gold sample despite our measurement of $z_{grism} = 1.95$ because it is still not known whether 12.3 is the correct counter-image to 12.1 and 12.2, both of which lack spectroscopic confirmation.

[e] The spectroscopic redshift of system 14 was reported erroneously by Jauzac et al. (2014) at $z = 2.0531$ using incomplete CLASH-VLT data. We measured $z_{grism} = 1.63$ for all three images in the system, in agreement with the redshift obtained using the complete CLASH-VLT data (Grillo et al. 2015, I. Balestra 2016, private communication).

[f] The redshift of this object was reported at $z_{grism} = 2.18 \pm 0.01$ ($Q = 3$) in the original GLASS catalog based on two marginal emission lines, but while preparing the manuscript Caminha et al. (2016) published a redshift of $z = 3.238$ from bright Lyα, which ruled out the grism redshift.

[g] Balestra et al. (2016) published their spectroscopic redshifts after the HFF modeling teams graded the mulitple images into the Gold, Silver, and Bronze categories. We include them in this table for completeness and comparison with z_{grism}.

[h] 29.1 was originally assigned as a Gold image from GLASS spectroscopy, but further analysis after the samples were chosen revealed that the spectroscopic confirmation was too tenuous. Therefore, this object should not be considered to be spectroscopically confirmed.

(This table is available in its entirety in machine-readable form.)

obtained by the ASTRODEEP team (Castellano et al. 2016; Merlin et al. 2016). The ASTRODEEP photometric redshifts were obtained through χ^2 minimization using PEGASE 2.0 (Fioc & Rocca-Volmerange 1997). The ASTRODEEP catalogs were built after subtracting ICL emission and the brightest foreground galaxies from the images in order to maximize the efficiency of high-redshift source detection and to obtain unbiased photometry. The catalogs employed the seven HFF filters: F435W, F606W, F814W, F105W, F125W, F140W, and F160W, a HAWK-I *K*-band image (G. Brammer 2016, in preparation), and *Spitzer*/IRAC [3.6] and [4.5] channels. The ASTRODEEP catalogs used two different detection images to create separate photometric catalogs. One catalog used F160W as the detection image, whereas the other used a stacked NIR image. To maximize the number of multiply imaged galaxies that we could detect, we merged the two catalogs into a single photometric catalog for this work.

Combining the photometric redshift information for multiple images of the same source provides a tighter constraint than a single measurement. We used a hierarchical Bayesian method similar to that used in Wang et al. (2015) (see also Press 1997, pp. 49–60 and Dahlen et al. 2013) to combine each photometric redshift PDF $P_i(z)$ into a single $P(z)$ for each system. We used the peak of the combined $P(z)$ (hereafter referred to as z_{Bayes}) as input to the lens model. In summary, the hierarchical Bayesian method considers the concept of the probability that each input $P_i(z)$ is unreliable (p_{bad}). It uses an input $P_i(z)$ in the calculation of the combined $P(z)$ for the system if it is reliable, otherwise it uses a flat (noninformative) $P_i(z)$. The method then marginalizes over all values of p_{bad} using an assumed prior on p_{bad} to

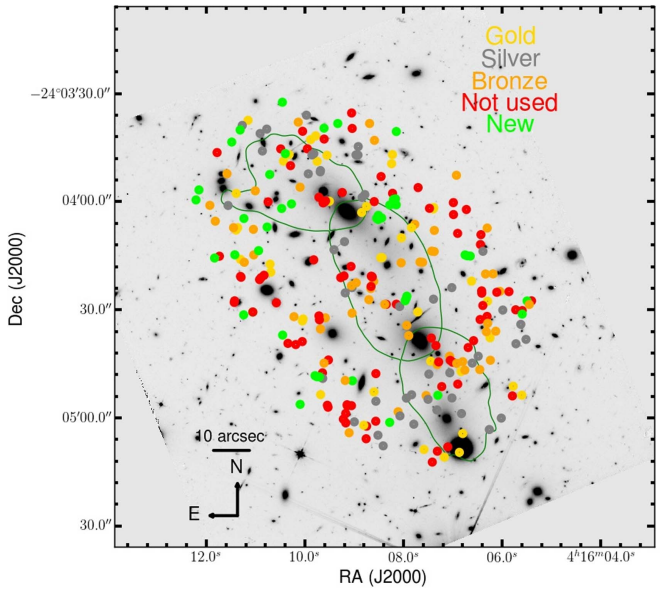

Figure 3. All multiple images discovered to date in MACS J0416. As indicated in the key, circles colored gold, gray and orange correspond to the multiple images in the Gold, Silver and Bronze samples, respectively (Section 4). Red circles correspond to multiple images that the HFF modeling teams deemed were less secure than those in the Bronze sample so they were not used in the lens models. Green circles represent new multiple image candidates discovered after the grading effort took place. The dark green line is the critical curve from our best-fit lens model at $z = 2.36$, the mean source redshift of the multiple images that were used in our lens model. Shown is the coadded CLASH+HFF +GLASS F105W image.

calculate the posterior $P(z)$ for the entire system. We assume a flat prior in $p_{\rm bad}$ for $p_{\rm bad} \leqslant 0.5$, i.e., that each $P(z)$ has at least 50% chance of being informative. This has the effect that for some systems with two images, the posterior $P(z)$ of the system has a small but non-zero floor due to the contribution from a noninformative $P_i(z)$. Because the floor inflates the photometric redshift uncertainty, we subtract the floor from all posterior $P(z)$'s before calculating confidence intervals. Subtracting the floor does not change the peak redshift of the posterior $P(z)$.

4.2. GLASS Spectroscopy

Here we describe the procedure for measuring the redshifts of the multiply imaged galaxies using the GLASS spectra. The GLASS spectra of 272 multiple image candidates were carefully examined in order to identify features for redshift measurements. As a testament to the efficiency of the GLASS progam, this search resulted in the confident identification of spectroscopic redshifts for 13 new multiple images. Wang et al. (2015) similarly demonstrated this by securing the spectroscopic redshifts of five multiply imaged galaxies behind Abell 2744.

Each spectrum was visually inspected by multiple investigators (A.H., T.T., and A.B.) using the GLASS Graphical User Interfaces (GUIs) dubbed the GLASS Inspection GUI (GiG) and GLASS Inspection GUI for redshifts (GiGz[17]; Treu et al. 2015). Both P.A.s were inspected individually and then again once stacked together. The results were then combined to form a list of multiple images with identified emission lines. Following Treu et al. (2015) and Schmidt et al. (2016), a quality flag was given to the redshift measurement: $Q = 4$ is secure; $Q = 3$ is probable; $Q = 2$ is possible; $Q = 1$ is likely an artifact. As described in Treu et al. (2015), these quality criteria take into account the signal-to-noise ratio of the detection, the probability that the line is a contaminant, and the identification of the feature with a specific emission line. For example, $Q = 4$ is given for spectra where multiple emission lines are robustly detected; $Q = 3$ is given for spectra where either a single strong emission line is robustly detected and the redshift identification is supported by the photometric redshift, or when more than one feature is marginally detected; $Q = 2$ is given for a single line detection of marginal quality. As shown in Table 3, new spectroscopic redshifts were obtained for measurements of quality 4 and 3 only, consisting of 30 images in total, corresponding to 15 systems. Example spectra of $Q = 3$ and $Q = 4$ objects are shown in Figure 12.

The uncertainty in our spectroscopic redshift measurements is limited by the grism wavelength resolution of approximately 50 Å and by uncertainties in the zero point of the wavelength calibration. By comparing multiple observations of the same object we estimate the uncertainty of our measurements to be of the order of $\Delta z \lesssim 0.01$, similar to what was reported by Wang et al. (2015).

Some multiple images that we confirm with GLASS spectroscopy were previously spectroscopically confirmed by other authors. We compare the redshifts obtained in this work with those previously obtained, seeing agreement within the uncertainties for all multiple images except system 14. Images 14.1, 14.2, and 14.3 were originally reported to be spectroscopically confirmed at $z = 2.0531$ by Richard et al. (2014), using incomplete CLASH-VLT data. Grillo et al. (2015), using the complete CLASH-VLT data set for MACS J0416, recently reported redshifts of $z = 1.6370$ for images 14.1 and 14.2. We confirm the updated redshift measurements of 14.1 and 14.2 by Grillo et al. (2015) by identifying strong [O II]$\lambda\lambda$3727, 3729 and [O III]$\lambda\lambda$4959, 5007 + Hβ emission at $z_{\rm grism} = 1.63 \pm 0.01$ in the GLASS spectra of both images. In addition, we confirm 14.3 at $z_{\rm grism} = 1.63 \pm 0.01$ by identifying the same lines observed in the grism spectra of 14.1 and 14.2. We note that all v1 HFF lens models of the cluster that used system 14 used the incorrect spectroscopic redshift of $z = 2.0531$. During the revision process, Caminha et al. (2016) reported the redshifts of 15 multiple images with previous spectroscopic redshifts. All of these are in agreement with the redshifts confirmed herein, with the exception of multiple image 26.1. We had originally reported a $Q = 3$ redshift of $z = 2.19 \pm 0.01$ based on marginal detection of [O II] $\lambda\lambda$3727, 3729 and [O III]$\lambda\lambda$4959, 5007, which is in disagreement with the redshift of $z = 3.238$ from bright Lyα reported by Caminha et al. (2016). We therefore omit this object from our catalog, concluding that the marginal detections in the GLASS spectra were due to contamination residuals.

We report the redshifts of 12 new multiple images. We show the GLASS spectra for these objects in Appendix B. The complete set of spectra are available online as a figure set of 26 elements. The catalog of multiply imaged objects with GLASS redshifts is also publicly available (see footnote 3). We summarize our spectroscopic measurements for the 12 new images by system below:

1. System 5: Before the GLASS data were analyzed, none of the images in system 5 had published spectroscopic redshifts. We confirm all four images in the system as belonging to the same source galaxy at $z = 2.09 \pm 0.01$ based on the detection of [O III]$\lambda\lambda$4959, 5007 in both P.A.s of the G141 spectra of all four images. Hβ and [O II]

[17] Available at https://github.com/kasperschmidt/GLASSinspectionGUIs.

Table 3
GLASS Spectroscopic Results for Multiply and Singly "Imaged" Sources

ID_{GLASS}[a]	ID_{arc}	R.A. (deg.)	Decl. (deg.)	F140W (mag.)	z_{phot}[b]	z_{grism}	Quality	N_{lines}[c]	Line(s)	Magnification
268	2.1	64.04116	−24.06185	23.01 ± 0.01	…	1.90	4	3	[O II] Hβ [O III]	$8.26^{+0.97}_{-0.61}$
248	2.2	64.04304	−24.06305	23.08 ± 0.01	$2.4^{+0.1}_{-0.1}$	1.89	4	3	[O II] Hβ [O III]	$8.49^{+0.34}_{-0.70}$
572	2.3	64.04748	−24.06885	22.97 ± 0.01	$2.4^{+0.2}_{-0.3}$	1.90	4	3	[O II] Hβ [O III]	$4.13^{+0.29}_{-0.37}$
494	3.1; 4.1[c]	64.03080	−24.06720	23.32 ± 0.01	…	1.99	4	3	[O II] Hβ [O III]	$4.13^{+0.03}_{-0.09}$
372	3.2; 4.2	64.03518	−24.07098	23.13 ± 0.01	$2.5^{+0.1}_{-0.1}$	1.99	4	3	[O II] Hβ [O III]	$2.27^{-0.02}_{-0.06}$
955	3.3; 4.3	64.04185	−24.07581	23.21 ± 0.01	…	1.99	4	3	[O II] Hβ [O III]	$3.20^{+0.12}_{-0.01}$
519	5.1	64.03245	−24.06848	21.58 ± 0.00	…	2.09	4	3	[O II] Hβ [O III]	$14.37^{+0.24}_{-1.09}$
520	5.2	64.03264	−24.06866	23.78 ± 0.01	$2.4^{+0.1}_{-0.1}$	2.09	4	3	[O II] Hβ [O III]	$25.51^{+1.78}_{-1.25}$
584	5.3	64.03355	−24.06947	23.14 ± 0.01	$1.8^{+0.6}_{-0.4}$	2.10	4	3	[O II] Hβ [O III]	$4.47^{+0.24}_{+0.08}$
1031	5.4	64.04355	−24.07696	25.56 ± 0.05	$2.5^{+0.1}_{-0.2}$	2.09	4	2	Hβ [O III]	$2.55^{+0.00}_{-0.03}$
312	7.1	64.03981	−24.06310	24.89 ± 0.04	$2.3^{+0.2}_{-0.3}$	2.09	4	2	Hβ [O III]	$401.21^{+130.09}_{-310.13}$
321	7.2	64.04058	−24.06354	24.95 ± 0.03	…	2.09	3	1	[O III]	$14.51^{+0.36}_{-2.02}$
1033	10.1	64.02602	−24.07717	23.96 ± 0.02	…	2.29	3	3	[O II] Hβ [O III]	$8.47^{-0.11}_{-0.73}$
456	12.3[d]	64.02898	−24.06665	22.24 ± 0.01	$1.9^{+0.1}_{-0.1}$	1.96	4	0	…	$2.84^{+0.11}_{-0.00}$
889	14.1	64.02623	−24.07433	22.97 ± 0.01	…	1.63	4	3	[O II] Hβ [O III]	$4.58^{-0.09}_{-0.29}$
880	14.2	64.03104	−24.07896	22.92 ± 0.01	…	1.63	4	2	[O II] [O III]	$2.16^{+0.09}_{-0.15}$
1213	14.3	64.03583	−24.08132	22.74 ± 0.01	$1.7^{+0.2}_{-0.3}$	1.63	4	3	[O II] Hβ [O III]	$4.78^{+0.05}_{-0.29}$
957	15.1	64.02687	−24.07574	26.16 ± 0.07	$2.8^{+0.1}_{-0.2}$	2.34	3	1	[O III]	$15.01^{-0.43}_{-2.52}$
1186	16.1	64.02406	−24.08090	…	$2.2^{+6.1}_{-1.6}$	1.96	4	3	[O II] Hβ [O III]	$5.23^{+0.16}_{-0.10}$
1362	16.3	64.03160	−24.08577	23.65 ± 0.01	…	1.97	3	1	[O III]	$6.05^{+0.30}_{-0.27}$
1197	17.3	64.02335	−24.08158	…	…	2.23	4	3	[O II] Hβ [O III]	$4.27^{+0.05}_{-0.04}$
750	23.1	64.04454	−24.07208	24.22 ± 0.02	$2.4^{+0.1}_{-0.2}$	2.09	4	2	[O II] [O III]	$3.06^{+0.03}_{-0.03}$
332	23.3	64.03432	−24.06372	24.40 ± 0.02	$2.3^{+0.1}_{-0.2}$	2.09	4	1	[O III]	$4.09^{+0.03}_{-0.08}$
347	27.2	64.04746	−24.06601	23.49 ± 0.02	…	2.11	4	1	[O III]	$69.69^{+17.58}_{-2.07}$
394	28.1; 28.2[e]	64.03667	−24.06732	20.91 ± 0.00	$0.8^{+0.1}_{-0.1}$	0.94	4	1	Hα	$65.86^{+57.83}_{-11.08}$
753	29.3	64.04462	−24.07148	24.56 ± 0.03	$2.4^{+0.1}_{-0.2}$	2.28	4	1	[O III]	$3.40^{+0.04}_{-0.05}$
141	…	64.03330	−24.05824	24.94 ± 0.03	$0.8^{+0.1}_{-0.1}$	0.82	4	2	[O III] Hα	$1.59^{+0.01}_{-0.01}$
98	…	64.02949	−24.05639	25.68 ± 0.05	$2.6^{+0.2}_{-0.2}$	2.14	4	3	[O II] Hβ [O III]	$2.26^{-0.01}_{-0.07}$
94	…	64.03309	−24.05633	22.23 ± 0.01	$1.2^{+0.3}_{-0.1}$	1.36	4	3	[O II] [O III] Hα	$1.91^{+0.00}_{-0.03}$
90000	…	64.02515	−24.05637	21.70 ± 0.01	$0.3^{+0.2}_{-0.1}$	0.39	4	0	…	…
108	…	64.03986	−24.05719	24.80 ± 0.03	$2.5^{+0.1}_{-0.1}$	2.22	4	3	[O II] Hβ [O III]	$2.51^{+0.03}_{-0.01}$
90001	…	64.05564	−24.06030	…	$0.4^{+0.1}_{-0.2}$	0.41	4	0	…	…
155	…	64.02725	−24.05911	21.73 ± 0.00	$0.3^{+0.2}_{-0.1}$	0.37	4	0	…	…
451	…	64.05742	−24.06632	25.47 ± 0.04	$1.3^{+0.2}_{-0.2}$	1.35	4	4	[O II] [O III] Hα [S II]	$2.54^{-0.01}_{-0.05}$
90002	…	64.05920	−24.06649	17.97 ± 0.00	$0.3^{+0.1}_{-0.1}$	0.31	4	1	Hα	…
186	…	64.04089	−24.06035	20.02 ± 0.00	$0.4^{+0.1}_{-0.1}$	0.40	4	0	…	…

Notes. GLASS spectroscopic results for all mulitply "imaged" and the first 10 singly "imaged" galaxies. The full catalog of singly "imaged" galaxies confirmed by GLASS is available online. z_{phot} lists the best-fit and 68% confidence limits on the photometric redshift from the ASTRODEEP photometric catalog. z_{grism} is the grism spectroscopic redshift we measure in this work. The nominal uncertainty in z_{grism} is ∼0.01 for objects with $N_{lines} \geqslant 1$. However, the redshift uncertainty is more variable for objects with $N_{lines} = 0$, which were confirmed by fitting the continuum grism spectra to templates of spectral energy distribution (SED) (G. Brammer 2016, in preparation). Entries with quality 3 and 4 refer to probable and secure spectroscopic redshifts, respectively.

[a] Objects with ID_{GLASS} in the format 9XXXX come from an extraction based on a different source detection image than the one used to extract the other GLASS IDs.

[b] The images for which z_{phot} is not shown are either contaminated or not detected in the photometric catalog.

[c] Systems 3 and 4 are believed to be different subtructures of the same source galaxy due to the similar redshift and spatial position of the multiple images in each system.

[d] The uncertainty in z_{grism} for $ID_{arc} = 12.3$ is ∼0.02 rather than the nominal ∼0.01 because the redshift was obtained by fitting its continuum emission in the grism to SED templates rather than through the identification of emission lines.

[e] 28.1 and 28.2 were detected as the same object in the segmentation map used to extract the grism data.

(This table is available in machine-readable form.)

λλ3727, 3729 were also detected in 5.1, 5.2, and 5.3, consistent with $z = 2.09 \pm 0.01$. The CLASH-VLT team published a consistent redshift of $z = 2.092$ (Balestra et al. 2016) for image 5.2 after the HFF modeling team determined its samples using the GLASS spectra.

2. System 12: 12.3 was the only multiple image candidate inspected that showed significant continuum emission but no emission lines. It was confirmed to $z = 1.96 \pm 0.02$ by fitting its bright continuum emission in the GLASS spectra to template SEDs using the method described by G. Brammer (2016, in preparation).
3. System 15: 15.1 was confirmed to $z = 2.34 \pm 0.01$ by the detection of [O III]λλ4959, 5007 in both P.A.s of the G141 spectra.

4. System 23: 23.1 and 23.3 were confirmed to $z = 2.09 \pm 0.01$ by the detection of strong [O III]$\lambda\lambda$4959, 5007 in both P.A.s of the G141 spectra.
5. System 27: We detected [O III]$\lambda\lambda$4959, 5007 at $z = 2.11 \pm 0.01$ in both P.A.s of the G141 spectra of image 27.2.
6. System 28: 28.1 and 28.2 were detected as the same object in the GLASS catalog. The redshift was determined to be $z = 0.938^{+0.001}_{-0.002}$ by fitting to bright continuum and an extended emission line identified as Hα.
7. System 29: 29.3 was confirmed by detecting [O III] $\lambda\lambda$4959, 5007 at $z = 2.28 \pm 0.01$ in both G141 P.A.s.

4.3. Search for Additional Systems

We also conducted a search for line emitters among known sources within the entire FOV of the grism. Two coauthors (A. B. and T.T.) visually inspected all of the 2D grism spectroscopic data products, the contamination models, and residuals after subtraction of contamination. We attempted to identify new multiple systems among the galaxies with the same grism spectroscopic redshifts but did not find any. Some of them are ruled out because of the relative positions of the multiple images in the cluster, while others are ruled out because their distinct colors and morphologies are inconsistent with being the same source.

We compiled a list of singly imaged galaxies with redshifts determined from both emission line and absorption features, consisting of four spectroscopic redshift measurements of quality 3 and 166 of quality 4, which are color-coded in Figures 1 and 2 and listed in Table 3. Using the photometric catalog described above, we measure the photometric redshifts of these objects and compare them with the spectroscopic redshifts in Figure 4. Of the objects for which photometric redshifts could be measured, we find that approximately 66% (57/86) of the photometric redshifts agree with their spectroscopic redshifts within the 68% confidence intervals. This suggests that the photometric redshift errors are reliably estimated.

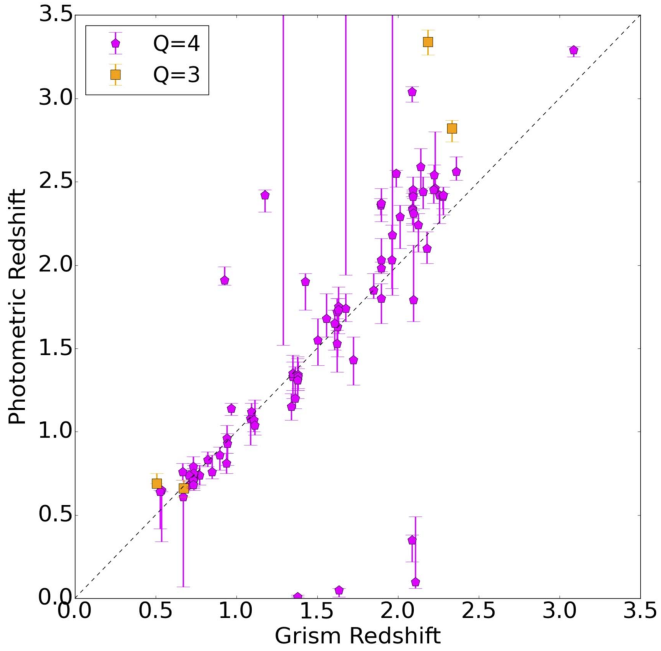

Figure 4. Comparison between the grism and photometric redshifts for the 86 objects with high-confidence emission lines (quality flags 4 (magenta pentagons) or 3 (orange squares)) for which photometric redshifts could be measured. Error bars on the photometric redshifts are 1σ (enclosing 68% of the total probability). There is good statistical agreement between photometric and grism redshifts, with 57/86 (66%) of the grism redshifts within the photometric redshift error bars. This suggests that the photometric redshift errors are well estimated. The dotted black line represents perfect agreement between photometric and grism redshifts.

5. GRAVITATIONAL LENS MODEL

Our lens modeling method, SWUnited (Bradač et al. 2005, 2009), constrains the gravitational potential of a galaxy cluster via an iterative χ^2 minimization algorithm. It takes as input a simple initial model for the potential. After each iteration, a χ^2 is calculated from strong and weak gravitational lensing data on an adaptive, pixelated grid. The number of grid points is increased at each iteration, and the χ^2 is recalculated. Once the minimum is found, and convergence is achieved, derivative maps of lensing quantities, such as convergence (κ), shear (γ), and magnification (μ), are produced from the best-fit potential map.

5.1. Weak Lensing Galaxies

While the strong lensing constraints on the lens model are already described in (Section 4), the weak lensing catalog is based on the ACS/WFC F606W observations (~30 ks) of the cluster from the HFF program. For the reduction and the generation of the weak lensing catalog we make use of the pipeline described by Schrabback et al. (2010), which employs the KSB+ formalism (Kaiser et al. 1995; Luppino & Kaiser 1997; Hoekstra et al. 1998) for measurements of galaxy shape as detailed by Erben et al. (2001) and Schrabback et al. (2007).

We model the spatially and temporally variable ACS PSF using the approach of principal component analysis from Schrabback et al. (2010). These authors find that ~97% of the total variation in ACS PSF ellipticity can be accounted for using a model with a single free parameter that is related to the *HST* focus position. We calibrate this model using more recent ACS stellar field observations taken in the F606W filter (see T. Schrabback et al. 2016, in preparation for details). We then fit the ellipticities and half-light radii of stars in the cluster field using this model. Here we estimate separate best-fitting models for each contributing cluster field exposure to optimally account for the temporal PSF variations. For the stack the spatially varying model is then computed from the combination of all single-exposure models, taking their relative shifts and rotations into account.

A major difference from Schrabback et al. (2010) is the application of the pixel-based correction for charge-transfer inefficiency (CTI) developed by Massey et al. (2014). Further details on the recent modifications to the pipeline are provided by T. Schrabback et al. (2016, in preparation), including a new verification test for the CTI correction in the context of studies of cluster weak lensing and updates for the weighting scheme employed for weak lensing.

The resulting shape catalog contains 1827 members. This catalog is first cross-matched with the ASTRODEEP photometric catalog, which is obtained from the HFF images (limiting AB magnitude ~29 in each band; see Section 4.1). Galaxies with a match in the ASTRODEEP catalog are individually assigned a redshift using the "ZBEST" keyword

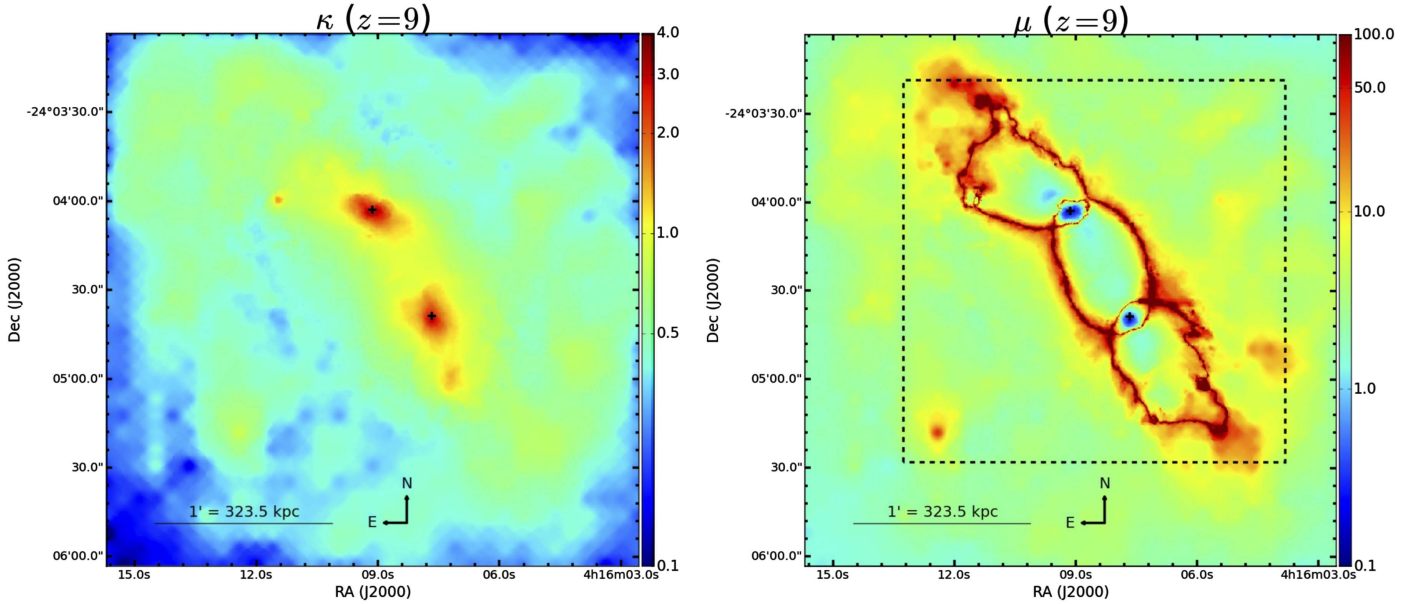

Figure 5. Left: convergence (κ) map of MACS J0416 produced by our lens model for a source at $z_s = 9$. The convergence map reveals two primary peaks in the total mass density, centered approximately at the location of the two BCGs, which are marked by the two black crosses. Right: flux magnification (μ) map of MACS J0416 produced by our lens model for a source at $z_s = 9$. The approximate location of the critical curve—the curve along which magnification is maximized—can be seen. The dotted black square outlines the common area over which magnification maps were produced by all collaborative HFF modeling teams (see Section 5.2; Figure 6). Both the convergence and the magnification maps reveal a highly elliptical total mass distribution, as found by several other authors (e.g., Zitrin et al. 2013; Jauzac et al. 2014). Both maps cover the same 3.0×3.0 arcmin^2 footprint. The two black crosses on each map mark the centers of the two BCGs determined from the F105W image. Note that the color bar has a logarithmic scale.

from the ASTRODEEP catalog. Because the coverage in F606W is larger than in WFC3/IR, only 710 galaxies of the 1827 galaxies in the shape catalog have counterparts in the ASTRODEEP catalog. We cross-match the remaining galaxies with the CLASH photometric catalog, in which objects are detected in the stacked ACS+WFC3/IR bands. The CLASH catalog is based on the pre-HFF *HST* images that are approximately 2 mag shallower per band than the post-HFF images. 698 of the remaining galaxies from the shape catalog are successfully matched to objects in the CLASH catalog. The CLASH photometric catalogs use the Bayesian Photometric Redshifts (BPZ) code (Benítez 2000; Coe et al. 2006). We use "z_b," the most likely redshift given by BPZ, to estimate the redshifts of the weak lensing galaxies. Finally, for galaxies matched to the ASTRODEEP and CLASH catalogs, we only use galaxies with an estimated redshift $z > z_{\rm cluster} + 0.2$ to ensure that the weak lensing catalog contains only background galaxies. 883 galaxies pass this redshift cut, resulting in a weak lensing source density of $\sim$100 galaxies arcmin^{-2}. This is comparable to the source density achieved by Jauzac et al. (2015a), who performed a similar measurement of the weak lensing signal from the HFF F814W image. This is a factor of $\sim$2 improvement in the source density achieved by using CLASH imaging alone.

The resulting maps of the convergence and magnification for a source at $z = 9$ are shown in Figure 5. The convergence map exhibits two peaks, roughly centered at the positions of the two BCGs. Smaller substructures can be seen to the northeast of the NE BCG and to the south of the SW BCG. These substructures have obvious luminous counterparts, which correspond to massive cluster galaxies visible near the two BCGs in Figure 3. The magnification map shows that the critical curve—the curve along which the magnification is maximized—is very elliptical. The magnification reaches values up to $\mu \sim$ 10–20 within a few arcseconds from the critical curve and values of $\mu \sim$ 1–2 near the edge of the HFF footprint. Typical values of the magnification are $\mu \sim$ 1–5 throughout the HFF footprint.

5.2. Comparison with Previous Work

A previous model of MACS J0416 using pre-HFF data was created using the same lens modeling code used in this work. The previous model was created in response to a call by STScI to model the HFF clusters before the HFF images were taken. The previous model appears on the publicly accessible HFF lens modeling website as the Bradač v1 model.[18] Our previous model was constrained using a total of 46 multiple images belonging to 12 distinct systems, as opposed to the 72 images and 26 systems used in the model presented here, which is made available to the public on the HFF lens modeling website as the Bradač v3 model. Only a few modeling teams produced v2 lens models of MACS J0416. The v2 HFF models were submitted to STScI during the time between the two official calls for lens models. Because our team submitted lens models exclusively during the official lens modeling calls, only Bradač v1 and v3 models exist of MACS J0416. In the v1 model, magnification uncertainties were estimated by bootstrap-resampling the weak lensing galaxies. In this work, however, we took a different approach to estimate uncertainties, one that we expect more accurately represents the statistical uncertainties. Because the number of multiple image systems used in this model is a factor of 2 larger than in the v1 model, we bootstrap-resampled all of the multiple image systems used in the model that were not spectroscopically confirmed. These are the systems for which we use $z_{\rm Bayes}$ in the lens model. We assessed the impact of photometric redshift uncertainty on the derived lensing quantities by resampling the redshift of each system

[18] http://www.stsci.edu/hst/campaigns/frontier-fields/Lensing-Models

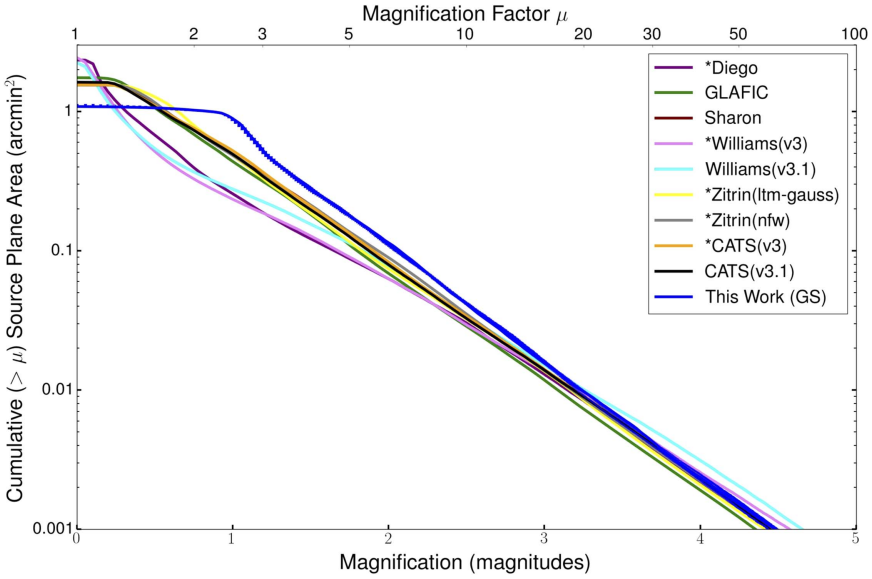

Figure 6. Cumulative source plane area ("cumulative area") vs. magnification at $z = 9$ for the lens model determined in this work (Bradač v3) and the other nine v3 HFF lens models. Model names preceded by "*" indicate models using the same sample of multiply imaged galaxies as used in this work, although the redshifts of the galaxies lacking spectroscopic confirmation have been estimated differently (see Section 5.2 for more details). The models are in general agreement at large magnifications ($\mu \gtrsim 5$). This is not surprising given that the constraints on multiple image appear in the regions with large magnification near the core of the mass distribution. There is significant disagreement among the models at $1 \lesssim \mu \lesssim 5$. These values of magnification are indicative of the outskirts of the modeled area of the cluster, where constraints come from weak lensing alone. Error bars are plotted for our model only and represent 68% confidence in the cumulative area.

lacking spectroscopic confirmation from their full $z_{\rm Bayes}$ posteriors. We exclude values of the redshift $z < z_{\rm cluster} + 0.1$ when resampling from the $z_{\rm Bayes}$ posteriors. We compare the variance in magnification due to redshift uncertainty with the variance in magnification due to bootstrap-resampling the multiple image systems, finding that the latter is dominant. We nonetheless propagate both sources of error when reporting the errors on all derived lensing quantities in this work. Systematic uncertainties are not accounted for in our error analysis.

Six other teams (CATS, Sharon, Zitrin, Williams, GLAFIC, and Diego, as they appear on the HFF lens modeling page) created new lens models of the HFF clusters, which have also been made available to the public on the HFF lens modeling website (see footnote 18). The lens models were released to the public on 2015 December 4 while we were preparing this manuscript, but after we had completed the lens model of the cluster. All teams had access to the same constraints on multiple images, including the spectroscopic constraints from GLASS described herein. The CATS (v3), Diego, Zitrin (nfw and ltm-Gauss), and Williams (v3) models use the same Gold and Silver multiple images that we used to constrain our model. The CATS (v3.1), Williams (v3.1), and GLAFIC models use Gold, Silver, and Bronze images, and the Sharon model uses only the Gold images. We expect that the four models that used Gold and Silver images are the most directly comparable to our lens model.

While the determination of the Gold, Silver, and Bronze samples was coordinated among the modeling teams, each team independently determined the redshifts of the Silver (and Bronze) images. As a result, no two models, with the exception of the Zitrin nfw and ltm-Gauss models, share exactly the same constraints on multiple images. This should be kept in mind when comparing the models.

We first compare the cumulative magnified $z = 9$ source plane area (cumulative area, hereafter) predicted by all models in Figure 6. The predictions of cumulative area among the nine models are significantly different for magnifications in the range $1 \lesssim \mu \lesssim 5$. As shown in Figure 5, the region with $1 \lesssim \mu \lesssim 5$ is primarily in the outskirts of the field, several hundred kiloparsecs from the critical curve. At this distance from the critical curve, weak lensing galaxies provide the only constraints to our model, because the strength of the lens is not sufficient to multiply image background galaxies. None of the other nine v3 or v3.1 models uses weak lensing constraints, but instead they rely on an extrapolation of the core region to predict the magnification in the outskirts. Therefore, the disagreement between the models, and in particular with ours, is not surprising in this regime.

We assess whether the use of different sets of images could be responsible for the difference, but find that it is not likely the case. The models that similarly used the Gold and Silver samples of multiple images are still in disagreement in this regime. Further, the CATS and Williams teams constructed two models of the cluster. The v3 models of both teams use the Gold and Silver images only, whereas the v3.1 models use the Gold, Silver, and Bronze samples. For each of these teams, the cumulative areas predicted by the v3 and v3.1 models are very similar over a large range of magnifications ($1 < \mu < 100$), despite the v3.1 models using an additional 58 Bronze images. We also test whether the choice of our initial model could bias our model predictions. The prediction from our initial model is significantly different from the prediction from our reconstructed model. In fact, the initial model is more similar to the CATS, GLAFIC, and Zitrin models for magnifications in the range $1 \lesssim \mu \lesssim 5$, and it is driven away from these models during the minimization.

There is general agreement among the models for cumulative areas at $\mu \gtrsim 5$. This is reassuring because the region of the cluster for which $\mu \gtrsim 5$ is near the critical curve, which is primarily constrained by the multiply imaged galaxies, which are numerous for this cluster. The image plane area used to make the plots of cumulative area was the common area shared by all nine magnification maps, and is shown as the dashed box

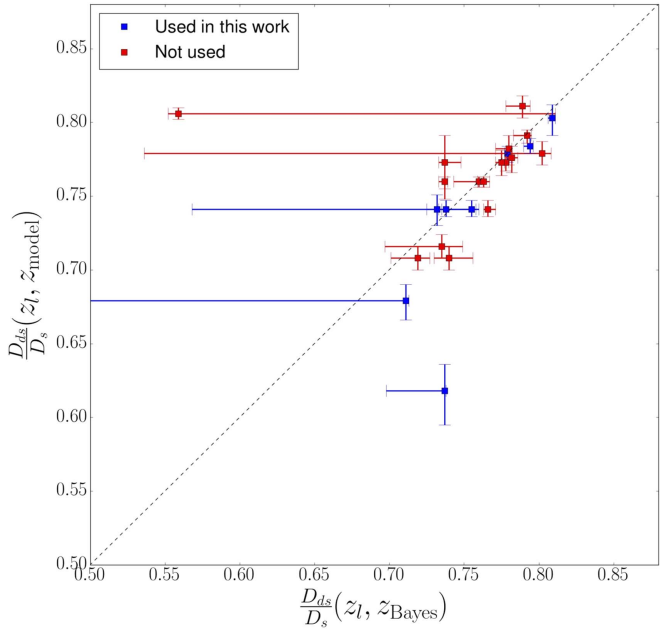

Figure 7. Comparison of the ratio of angular diameter distances, the quantity with which the lensing deflection scales, for redshifts of multiply imaged galaxies determined in this work ($z_{\rm Bayes}$) vs. the redshifts predicted by the CATS v3.1 model ($z_{\rm model}$; M. Jauzac et al. 2016, in preparation). The CATS v3.1 model used Gold+Silver+Bronze images, whereas we used only Gold +Silver images in our lens model, although we calculate $z_{\rm Bayes}$ for all three categories to improve the statistics for this comparison. Gold+Silver images are the blue points, and the Bronze images are the red points. The vertical error bars were obtained by resampling from the 1σ Gaussian errors on $z_{\rm model}$. The horizontal error bars represent 68% confidence and were obtained by resampling from $P(z_{\rm Bayes})$. The asymmetric horizontal error bars arise because $P(z_{\rm Bayes})$ is multi-modal for those multiply imaged galaxies. There is overall good agreement between $z_{\rm Bayes}$ and $z_{\rm model}$. The dotted black line is shown for reference and represents perfect agreement.

in the right panel of Figure 5. This area was set by the Williams magnification maps, which cover approximately 4.65 arcmin^2.

Although different modeling teams used different sets of multiply imaged galaxies, it is difficult to see how this directly affects the models from Figure 6 alone. The factor with which the deflection angle scales for a source at $z = z_{\rm Bayes}$ is the ratio of the angular diameter distances, $\frac{D_{\rm ds}}{D_{\rm s}}(z_{\rm l}, z_{\rm s})$, where $D_{\rm ds}$ is the angular diameter distance between the lens at $z = z_{\rm l}$ and the source at $z = z_{\rm s}$, and $D_{\rm s}$ is the angular diameter distance between $z = 0$ and $z = z_{\rm s}$. It is therefore the factor in which the source redshift for a multiple image system directly enters the lens model. In Figure 7, we compare this ratio for redshifts estimated in this work with those predicted by the CATS v3.1 lens model. We choose to compare to the CATS v3.1 model because it uses Gold, Silver, and Bronze images and therefore provides the largest number of redshifts with which we can compare our photometric redshifts. The comparison is done for multiple image systems for which no spectroscopic redshift has been measured, whether in this work or previously. In this way, no spectroscopic redshift could be used as a prior for predicting the redshift. In the figure, $z_{\rm model}$ is the redshift that the CATS team obtained by optimizing their lens model while leaving the redshift as a free parameter. Overall, $z_{\rm Bayes}$ and $z_{\rm model}$ agree within the uncertainties. Wang et al. (2015) reached a similar conclusion by comparing $z_{\rm Bayes}$ and $z_{\rm model}$ for the multiple images predicted by the CATS v2 lens model of the HFF cluster Abell 2744. This is encouraging because similar inputs to the models allow a more direction comparison of the results.

6. STELLAR MASS FRACTION

6.1. Map of Stellar Mass Density

The lens model provides an estimate for the total mass density of the cluster, composed of mostly invisible dark matter. A fractional component of the total mass density comes from stars and can be inferred from the observed stellar light, independently of the lens model. The *Spitzer*/IRAC 3.6 μm image samples close to rest-frame K-band for the cluster, so we use the 3.6 μm fluxes from cluster members to estimate the distribution of cluster stellar mass. The cluster members come from the selection by Grillo et al. (2015), consisting of 109 spectroscopically confirmed and 66 photometrically selected cluster members.

To create an image with 3.6 μm flux from cluster members only, we first create a mask with value 1 for pixels that belong to cluster members in the F160W image and 0 otherwise. We then convolve the mask with the 3.6 μm PSF to match the IRAC angular resolution, set the pixels below 10% of the peak value to zero, and resample the mask onto the IRAC pixel grid. We obtain the 3.6 μm map of cluster members by setting all IRAC pixels not belonging to cluster members to zero and smoothing the final map of surface brightness with a two-pixel wide Gaussian kernel.

The map of IRAC surface brightness is transformed into a map of stellar surface mass density (stellar mass density map, hereafter) by the following procedure. We first convert the observed 3.6 μm flux into a map of rest-frame K-band luminosity after applying a -0.31 mag K-correction. The K-correction is derived using a passively evolving stellar population template from Bruzual & Charlot (2003) with an age of 9 Gyr, roughly the age of the universe at the cluster redshift. The luminosity map is then multiplied by the stellar mass to light ratio derived by Bell et al. (2003) using the so-called "diet" Salpeter stellar initial mass function (IMF), which has 70% of the mass of the IMF of Salpeter (1955) because there are fewer stars at low masses. Bell et al. (2003) obtained a stellar mass to light ratio of $M_\star/L_K = 0.95 \pm 0.26\, M_\odot/L_\odot$ in the stellar mass bin $10 < \log(M_\star h^2) < 10.5$. Their $M_\star/L_K$ values are insensitive to the chosen stellar mass bin. The ~30% error on $M_\star/L_K$ is the largest source of statistical uncertainty in the stellar mass density map.

The main source of systematic uncertainty in the stellar mass density map is the unknown IMF. For example, if we adopt the IMF of Salpeter (1955), as suggested by studies of massive early-type galaxies, the stellar mass density increases by a factor of 1.55 everywhere. We also assess the selection of cluster members as a source of systematic uncertainty. Grillo et al. (2015) estimate that their cluster member catalog is $\gtrsim$95% complete down to a stellar mass of $\log(M_\star/M_\odot) \simeq 9.8$ within the CLASH F160W footprint. We estimate the fraction of stellar mass density not included in our analysis due to the incomplete selection of cluster members at lower stellar masses. To do this, we compare the integral of the stellar mass function obtained by Annunziatella et al. (2014) for MACS J1206.2-0847, a different CLASH cluster at redshift $z = 0.44$, over the range of complete stellar masses from the selection of Grillo et al. (2015) with the integral over all stellar masses. We find that we exclude only ~3% of the stellar mass within the F160W footprint from CLASH as a result of the incomplete selection of cluster members. Figure 8 illustrates this by showing the cumulative stellar mass of the stellar mass

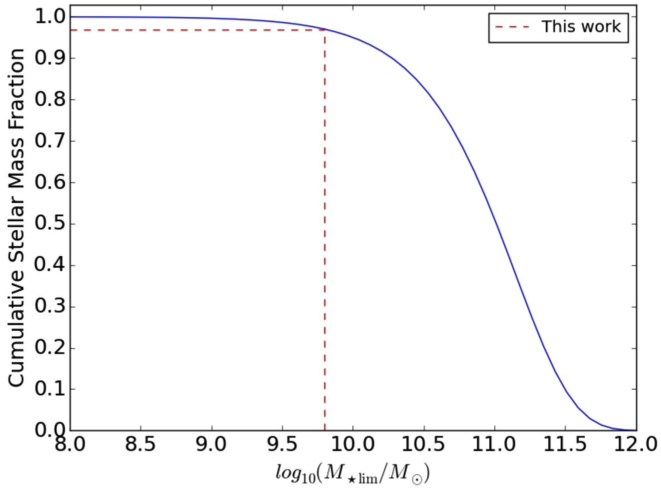

Figure 8. Cumulative stellar mass fraction as a function of the stellar mass limit. The cumulative stellar mass fraction (blue line) is estimated using the stellar mass function of Annunziatella et al. (2014). The stellar mass limit of the cluster member catalog used in this work (red dashed line) is $log_{10}(M_{\star\,\mathrm{lim}}/M_{\odot}) \simeq 9.8$, corresponding to a stellar mass fraction of ∼97%. We therefore estimate that only ∼3% of the total stellar mass is lost in our analysis due to the incomplete cluster member catalog.

function of Annunziatella et al. (2014) as a function of the stellar mass limit. Grillo et al. (2015) select cluster members down to $\log(M_{\star}/M_{\odot}) \simeq 8.6$, yet with <95% completeness in the stellar mass range $8.6 \lesssim \log(M_{\star}/M_{\odot}) \lesssim 9.8$. Therefore, the ∼3% estimated loss in stellar mass is a slight overestimate of the loss due to the incomplete selection of cluster members.

To justify our use of the $z = 0.44$ stellar mass function to estimate the stellar mass lost in MACS J0416 at $z = 0.396$, we assess the evolution of the stellar mass function in clusters over cosmic time and how such an evolution might impact our estimate of the fraction of stellar mass that we missed in our analysis. Studies of the evolution of the stellar mass function (e.g., Vulcani et al. 2011) find that it does evolve, but on timescales much longer than the ∼300 Myr elapsed between $z = 0.44$ and $z = 0.396$. For this reason, we consider the use of the stellar mass function obtained by Annunziatella et al. (2014) to be reliable for the estimation of the stellar mass not included in our analysis due to incompleteness of cluster members.

The presence of the ICL, when not accounted for, can also cause the stellar mass density to be underestimated (e.g., Gonzalez et al. 2013). Burke et al. (2015) recently measured the fraction of total cluster light contained in the ICL for 13/25 CLASH clusters, including MACS J0416. For MACS J0416, they found that $(2.69 \pm 0.10)\%$ of the total cluster light is contained in the ICL. Both the incompleteness of stellar mass and the ICL act to decrease the measured stellar mass density. Both effects, however, are an order of magnitude smaller than the uncertainty due to the IMF and the stellar mass to light ratio obtained by Bell et al. (2003).

6.2. Stellar to Total Mass Ratio

We obtain the map of projected stellar to total mass ratio ($f_{\star}$, hereafter) by dividing the stellar mass density map obtained from photometry by the total surface mass density map (total mass density, hereafter) obtained from our lens model. Before division, we match the resolutions of the two maps. The resolution of the stellar mass density map is controlled by the resolution of the *Spitzer*/IRAC 3.6 μm imaging, which is roughly uniform across the field. On the other hand, the resolution of the total mass density varies considerably across the field as a result of two processes that occur during the lens modeling procedure. The first effect is regularization, which globally degrades the resolution of the total mass density map. In order to estimate the decrease in resolution due to regularization, we used a simulated galaxy cluster designed to match the data quality of the HFF, Hera (Meneghetti et al. 2016). We made our own lens model of Hera that includes the effects of regularization, and we compare this with the correct lensing maps from the simulation. The correct simulated lensing maps are of a uniform resolution that is higher than the resolution of our lensing maps. To determine the global resolution correction, we variably degrade the resolution of the simulated convergence map until we find the best match to our reconstructed convergence map. The second effect is non-uniformity in the grid introduced by the lens modeler to match the signal-to-noise ratio of the lensing measurements (Bradač et al. 2009). The process of increasing the resolution in this manner will be referred to as refinement hereafter. Each pixel in the lensing map has an associated refinement level. The refinement grid for MACS J0416 has four levels: 1, 2, 4, and 8. Level 1 refinement represents no refinement and is reserved for the outskirts of the cluster. Level 8 refinement, which divides a single pixel into 8 × 8 pixels, is applied in a circular region centered on the multiple images used in the lens model with radii equal to 2.4 arcsec. Refinement levels 2 and 4 are used to mitigate discontinuities between level 1 and level 8 refinement. Refinement level 4 is used around the NE and SW BCGs in circles of radii 0.6 and 0.45 arcmin, respectively.

To match the resolution of the stellar mass density map to that of the total mass density map from our lens model, we convolve the stellar mass density map with a Gaussian kernel of spatially varying width. We vary the kernel width according to the level of refinement at each pixel. The kernel width in regions of refinement level 2 is always half the width of the kernel used in regions of refinement level 1. Likewise, the kernel widths in refinement levels 4 and 8 are always $\frac{1}{4}$ and $\frac{1}{8}$ of the width of the kernel used in regions of refinement level 1, respectively. We vary the kernel width of refinement level 1 from 0 to 1 arcmin and assess the squared difference in the convergence in our reconstruction and the simulated map, finding a best-fit kernel width of 0.75 arcmin in the region of refinement level 1. The stellar mass density map is convolved with the four different kernels in the four refinement regions determined by this value alone. The resulting resolution-corrected stellar mass density map is shown in the left panel of Figure 9.

The $f_{\star}$ map is shown in the right panel of Figure 9. There is significant variation in $f_{\star}$ throughout the cluster. While $f_{\star}$ reaches as high as ∼0.03 in some places, the global mean within the stellar mass-complete region of the map is 0.009 ± 0.003 (stat.; 68% confidence), after adding in a $(2.69 \pm 0.10)\%$ ICL contribution to the stellar mass density determined by Burke et al. (2015).

The IMF is the largest source of systematic uncertainty. The choice of an IMF of Salpeter (1955) over the diet-Salpter IMF assumed in this work would lead to an increase in the stellar mass density map, and therefore in the $f_{\star}$ map, of ∼50%.

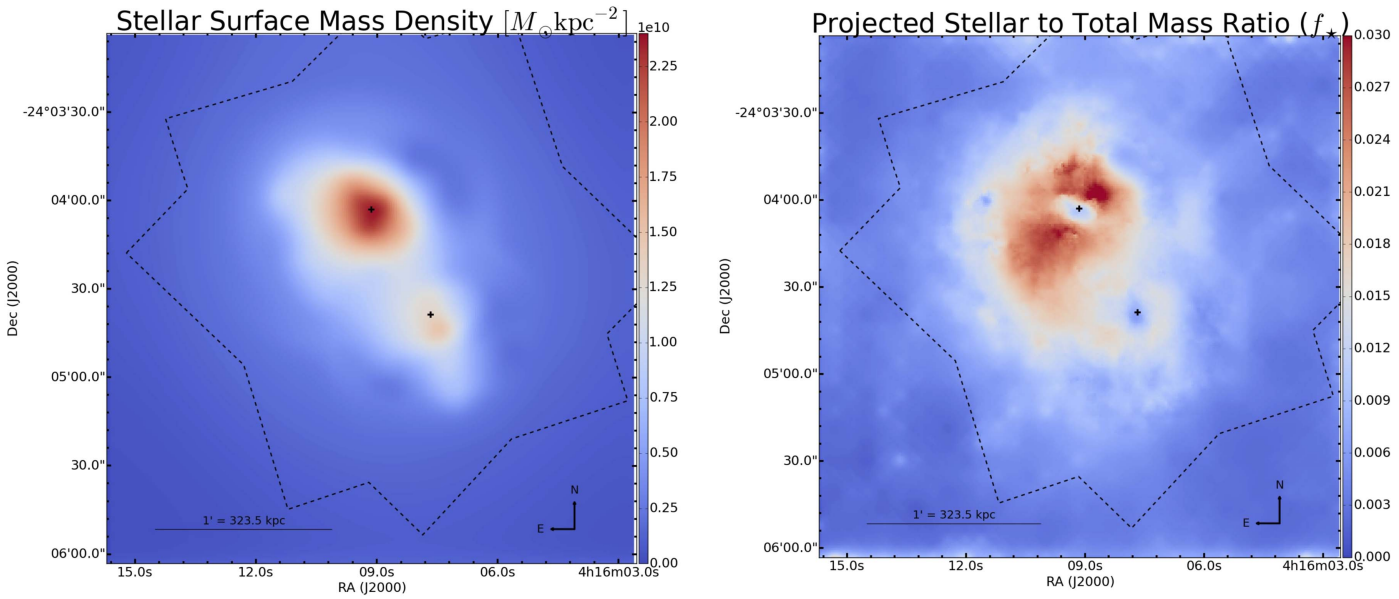

Figure 9. Left: stellar surface mass density (in units of $M_\odot$ kpc^{-2}) derived from a *Spitzer*/IRAC [3.6] image of MACS J0416. The resolution of this map has been matched to the resolution of the total surface mass density map by the "auto smoothing" approach described in Section 6.2. Right: projected stellar to total mass ratio ($f_\star$), obtained by dividing the stellar surface mass density (left panel) by the total surface mass density obtained from our lens model. The two black crosses on each map mark the centers of the two BCGs determined from the F105W image (see Figure 5). The drop in $f_\star$ at the locations of the BCGs is sensitive to our choice of smoothing technique and is significantly less pronounced if the "manual smoothing" approach is adopted when matching the resolution of the stellar mass density map to the total mass density map. (See Figure 10 for a direct comparison between the smoothing techniques.) The dotted black line in both panels shows the dithered F160W footprint from CLASH, which comprises ∼5.3 arcmin^2 of the entire 9 arcmin^2 FOV shown. The selection of cluster members conducted by Grillo et al. (2015) used to make the stellar surface mass density map is complete down to $\log(M_\star/M_\odot) \simeq 9.8$ in this region. Outside this region, the completeness and the uncertainty of both maps are not evaluated.

Another source of systematic error in $f_\star$ is the choice of cosmology, which affects both the stellar mass density and the total mass density. Cosmology impacts the stellar mass density through the distance modulus, which is used to convert the observed surface brightness of cluster members to physical surface brightness. Comparing the distance modulus calculated using our fiducial one-significant-figure concordance cosmology and a two-significant-figure cosmology from, e.g., Planck Collaboration (2015), we see a difference of ∼30%. The choice of cosmology has a much smaller effect on the total mass density. Cosmology impacts the total mass density through the critical surface mass density, $\Sigma_c = \frac{c^2 D_s}{4\pi G D_{ds} D_d}$. The difference in Σ_c is $\lesssim$3%. The effect of cosmology on Σ_c is not as significant as the effect on the distance modulus because it enters Σ_c in a ratio of angular diameter distances.

We also assess the potential systematic error resulting from smoothing the stellar mass density map to match the resolution of the total mass density map as described above. We show the dependence of $f_\star$ on the stellar surface mass density in Figure 10 for two different smoothing approaches. The "auto smoothing" method is the one described above. The "manual smoothing" approach differs from the previous approach in how we estimate the optimal kernel width at each refinement level. In the auto smoothing method, the kernel width in each refinement region is simply $1/\ell$ times the kernel width in refinement region 1, where ℓ is the refinement level. In the manual smoothing method, however, we determine the optimal kernel width in each refinement region separately. For each refinement level, we mask out the part of the convergence maps not refined at that level before comparing the squared difference in the simulated and reconstructed convergence maps for a range of kernel widths between 0 and 1 arcmin. In the regions corresponding to refinement levels 1 and 2, we find similar kernel widths using both smoothing methods. However, we find much smaller kernel widths in regions corresponding to refinement levels 4 and 8 when using the manual smoothing method. The stellar mass density map is smoothed significantly less near the BCGs in the manual smoothing approach. This effect is illustrated in Figure 10. In the auto smoothing approach, there is a downturn in $f_\star$ for stellar surface mass densities $\gtrsim 2 \times 10^{10} M_\odot$ kpc^{-2}. The downturn is significantly less pronounced in the manual smoothing approach, where the peaks of the stellar mass density are more preserved due to less smoothing. The right panel of Figure 9 shows $f_\star$ for the auto smoothing approach only. While the observed drop in $f_\star$ at the locations of the two BCGs is significant in this map, it is not significant in the map where the manual approach is used. The disparity in $f_\star$ between the auto and manual smoothing approaches at stellar surface mass densities $\gtrsim 2 \times 10^{10} M_\odot$ kpc^{-2} observed in Figure 10 provides an estimate of the systematic error in $f_\star$ as a result of smoothing the stellar mass density map.

Overall, however, the choice of smoothing approach only affects $\langle f_\star \rangle$ by 0.001, which is subdominant to the statistical error on $\langle f_\star \rangle$. The trend in $f_\star$ with stellar surface mass density for stellar surface mass densities $< 2 \times 10^{10} M_\odot$ kpc^{-2} is insensitive to the smoothing approach. This trend holds over ∼98% of the area of the stellar mass-complete region of the $f_\star$ map because values of the stellar surface mass density exceeding $2 \times 10^{10} M_\odot$ kpc^{-2} are rare, being observed only near the peaks of the two BCGs, as can be seen in the left panel of Figure 9. Thus our conclusion that there is considerable variation in $f_\star$ throughout the majority of the *HST* WFC3/IR FOV is also insensitive to the systematics associated with smoothing.

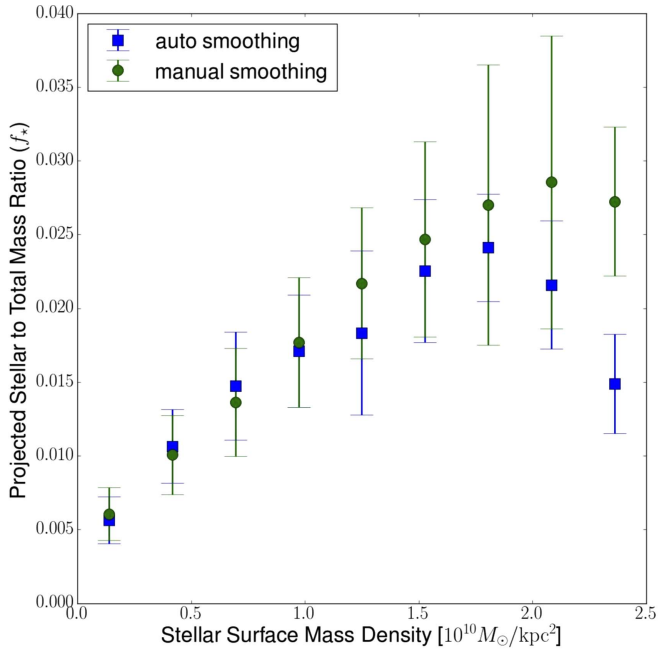

Figure 10. Projected stellar mass to total mass ratio ($f_\star$) vs. stellar surface mass density (in units of $10^{10}\,M_\odot\,\mathrm{kpc}^{-2}$) for the "auto" and "manual" smoothing approaches (described in Section 6.2) used to match the resolution of the stellar mass and total mass density maps. The data points and error bars represent the mean and standard deviation of all points falling in each of the nine equally spaced bins in stellar surface mass density. Only data from within the stellar mass-complete region shown in Figure 9 are displayed in this figure. The two different approaches provide an estimate of the systematic error associated with the resolution-matching procedure. The trend in $f_\star$ for stellar surface mass densities $<2\times10^{10}\,M_\odot\,\mathrm{kpc}^{-2}$ is bolstered by the agreement between the approaches in this regime. However, at the highest stellar surface mass densities in the cluster, which are found only near the cores of two BCGs, the two approaches disagree. Thus $f_\star$ is too uncertain at stellar surface mass densities $\gtrsim2\times10^{10}\,M_\odot\,\mathrm{kpc}^{-2}$ to conclude a downturn.

6.3. Comparison with Previous Work

We compare our value of $\langle f_\star\rangle$ with values obtained in the recent literature. In a similar analysis of MACS J0416 using strong and weak gravitational lensing, Jauzac et al. (2015a) measured $\langle f_\star\rangle = 0.0315 \pm 0.0057$ over the entire HFF F814W FOV. While there are a number of differences between our analyses, the key one is a difference of a factor of 2 in the total mass density maps obtained from lens modeling. Another important difference is their use of the IMF of Salpeter (1955), whereas we used the diet-Salpeter IMF. The passband used to derive the rest-frame K-band luminosity from cluster members is also different between our analyses. In this work, we used the *Spitzer*/IRAC 3.6 μm band, whereas Jauzac et al. (2015a) used F814W. Because *Spitzer*/IRAC 3.6 μm samples much closer to the rest-frame K-band than F814W, we expect that our estimate of L_K is an improvement over the measurement by Jauzac et al. (2015a). Jauzac et al. (2015a) used $M_\star/L_K = 0.99 \pm 0.03\,M_\odot/L_\odot$, which is consistent with our adopted value of $M_\star/L_K = 0.95 \pm 0.26\,M_\odot/L_\odot$. If we use the same IMF and value of $M_\star/L_K$ as Jauzac et al. (2015a), we find a value of $\langle f_\star\rangle = 0.014^{+0.005}_{-0.003}$, which is still a factor of ∼2 smaller than the value of $\langle f_\star\rangle$ found by Jauzac et al. (2015a). The discrepancy can be almost entirely accounted for by the difference in the total mass density maps; the mean total mass density predicted by our model is about a factor of 2 larger than that from the model of Jauzac et al. (2015a) within the F160W footprint, the area in which we calculate $\langle f_\star\rangle$. We note, however, that Jauzac et al. (2015a) obtained $\langle f_\star\rangle$ within a larger FOV, corresponding to the ACS/WFC.

Bahcall & Kulier (2014) measured $f_\star$ for $>10^5$ groups and clusters in the MaxBCG cluster catalog (Koester et al. 2007). Their cluster sample is taken from a photometric redshift range of $0.1 < z < 0.3$. Their $f_\star$ measurements cover a large range of scales (25 kpc to $30\,h^{-1}$ Mpc) and total masses ($M_{200} \sim 10^{13}$–$10^{15}\,M_\odot$), where M_{200} is the total mass within r_{200}, the radius within which the mean density is 200 times the critical density of the universe. On all scales larger than a few hundred kiloparsecs, Bahcall & Kulier (2014) measure a constant value of $\langle f_\star\rangle = 0.010 \pm 0.004$ (68% confidence). For the most massive clusters in their sample, which are most analogous to MACS J0416, they report a similar value of ∼1%. Bahcall & Kulier (2014) used stellar mass to light ratios calculated with i-band magnitudes from the Sloan Digital Sky Survey (SDSS; York et al. 2000) while employing a Chabrier IMF. In order to directly compare our results to Bahcall & Kulier (2014), we recalculated $\langle f_\star\rangle$ using F105W, the band with the smallest K-correction to the SDSS i-band at the redshift of MACS J0416, and then scaled the resulting light map using the same stellar mass to light ratio that they used, $M_\star/L_i = 2.5$. After recalculating, we obtain a value of $\langle f_\star\rangle = 0.012^{+0.005}_{-0.003}$ (stat.; 68% confidence), in agreement with the large-scale value obtained by Bahcall & Kulier (2014).

Gonzalez et al. (2013) measured $f_\star$ for 12 clusters at $z \sim 0.1$ over the mass range $M_{500} = (1\text{–}5) \times 10^{14}\,M_\odot$. They measured values of $f_\star$ ranging from 5% at the lower mass end of their sample to 1.5% at the upper mass end. Umetsu et al. (2014) recently measured $M_{500} = (7.0 \pm 1.3) \times 10^{14}\,M_\odot$ for MACS J0416. We recalculated $f_\star$ in the same band (WFPC2 F814W) and using the same stellar mass to light ratio as Gonzalez et al. (2013) ($M_\star/L_{F814W} = 2.65$), finding a value of $\langle f_\star\rangle = 0.014^{+0.005}_{-0.004}$ (stat.; 68% confidence). While MACS J0416 is at higher redshift ($z_{\mathrm{cluster}} = 0.396$) and has higher mass than the clusters studied by Gonzalez et al. (2013), our measured value of $\langle f_\star\rangle$ for MACS J0416 is comparable to the values measured by Gonzalez et al. (2013) at the highest masses. We also note that the area in which we calculate $f_\star$ is smaller than the area determined by r_{200}, the radius within which Gonzalez et al. (2013) measured $\langle f_\star\rangle$ for their cluster sample. Balestra et al. (2016) measure $r_{200} = 1.82$ Mpc for MACS J0416. Adopting this value of r_{200}, the region in which we measure $f_\star$ is $\sim0.4r_{200}$. We assumed a 30% error on the values of $M_\star/L$ (see Bell et al. 2003) when computing $\langle f_\star\rangle$ to compare to the values of $f_\star$ reported by Bahcall & Kulier (2014) and Gonzalez et al. (2013).

7. CONCLUSIONS

The massive galaxy cluster MACS J0416 is a powerful gravitational lens with excellent constraints for lens modeling. A coordinated search for multiple images of strongly lensed galaxies performed by several lens modeling teams found ∼200 candidate multiple images consisting of ∼100 source galaxies. In order to provide the best constraints to the many lens modeling teams, including our own, we inspected each of these candidate multiple images in the GLASS spectroscopy. Using GLASS spectroscopic measurements together with constraints obtained through the collaborative HFF modeling effort, we produced a gravitational lens model of MACS J0416. We then compared the projected stellar mass density map derived from IRAC photometry with the total mass density map obtained

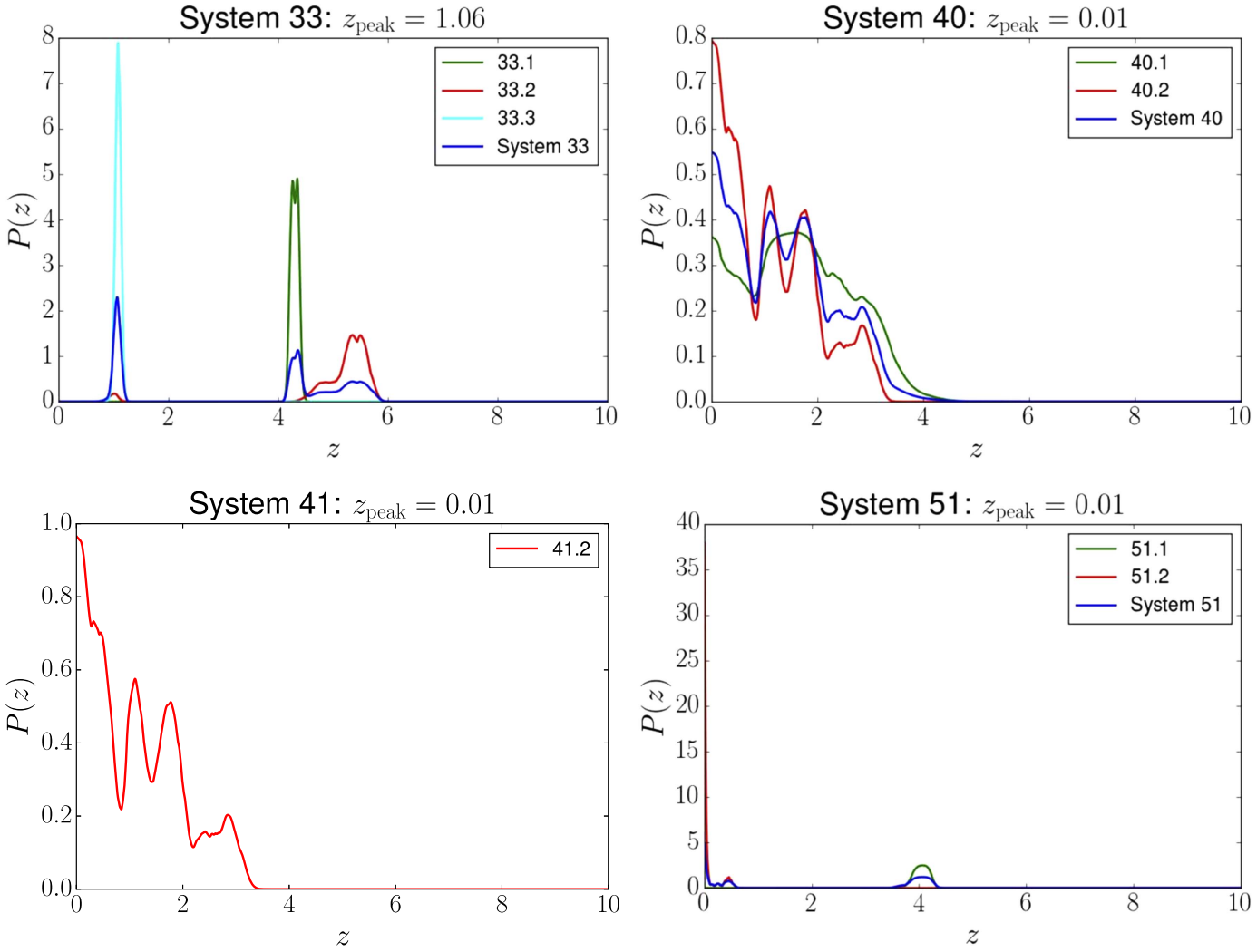

Figure 11. PDFs for the redshifts of multiple image systems in the Silver sample, which are too poorly constrained to use in the lens model. In all but the bottom left panel, the blue line represents the combined redshift ($z_{\rm Bayes}$) PDF, derived using the hierarchical Bayesian method developed by Dahlen et al. (2013). In system 41 (bottom left panel), only image 41.2 was detected in the photometric catalog, so multiple redshifts could not be combined. What is shown is the single PDF for the photometric redshift of 41.2, which is very poorly constrained.

from our lens model to study the projected stellar to total mass fraction throughout the cluster field. Our main results are summarized here.

1. We have measured spectroscopic redshifts for 30 multiple images (quality flag 3 (probable) and 4 (secure)), confirming five multiple image systems for the first time. The spectroscopically confirmed images were used to constrain our gravitational lens models and the nine other lens models discussed in this work. These lens models, including our own, are publicly available (see footnote 18).
2. We performed a visual search for faint emission and absorption lines, establishing a spectroscopic redshift catalog of lensed galaxies throughout the primary cluster field. We compared our photometric redshifts with grism spectroscopic redshifts and found good agreement, giving us more confidence in the photometric redshifts (and their errors) of the multiple images. We compared our photometric redshifts with redshifts determined from the v3.1 CATS lens model of MACS J0416 for the multiple images used in their lens model. We find general agreement with their redshifts.
3. The cumulative magnified source plane area ("cumulative area") predicted by our lens model was compared with the nine other lens models of MACS J0416 constrained using products from the same imaging and spectroscopy data. The predictions of cumulative area agree among the models for $\mu \gtrsim 5$ (mostly near the cluster core), but the results diverge among the models for the outlying regions with $\mu \lesssim 5$. We attribute the model differences to the lack of constraints in this region, with the exception of our model, which uses weak lensing constraints derived from the HFF imaging data. Despite the conservative approach of including only the Gold (spec-z) and Silver (high-confidence phot-z) multiple image systems identified by the HFF modeling collaboration, systematics from misidentification and redshift estimation of the Silver systems may influence the lens model. However, the inclusion of grism spectroscopic redshifts helps the lens modeling by providing stronger constraints and revising the incorrect redshifts used in the previous models.

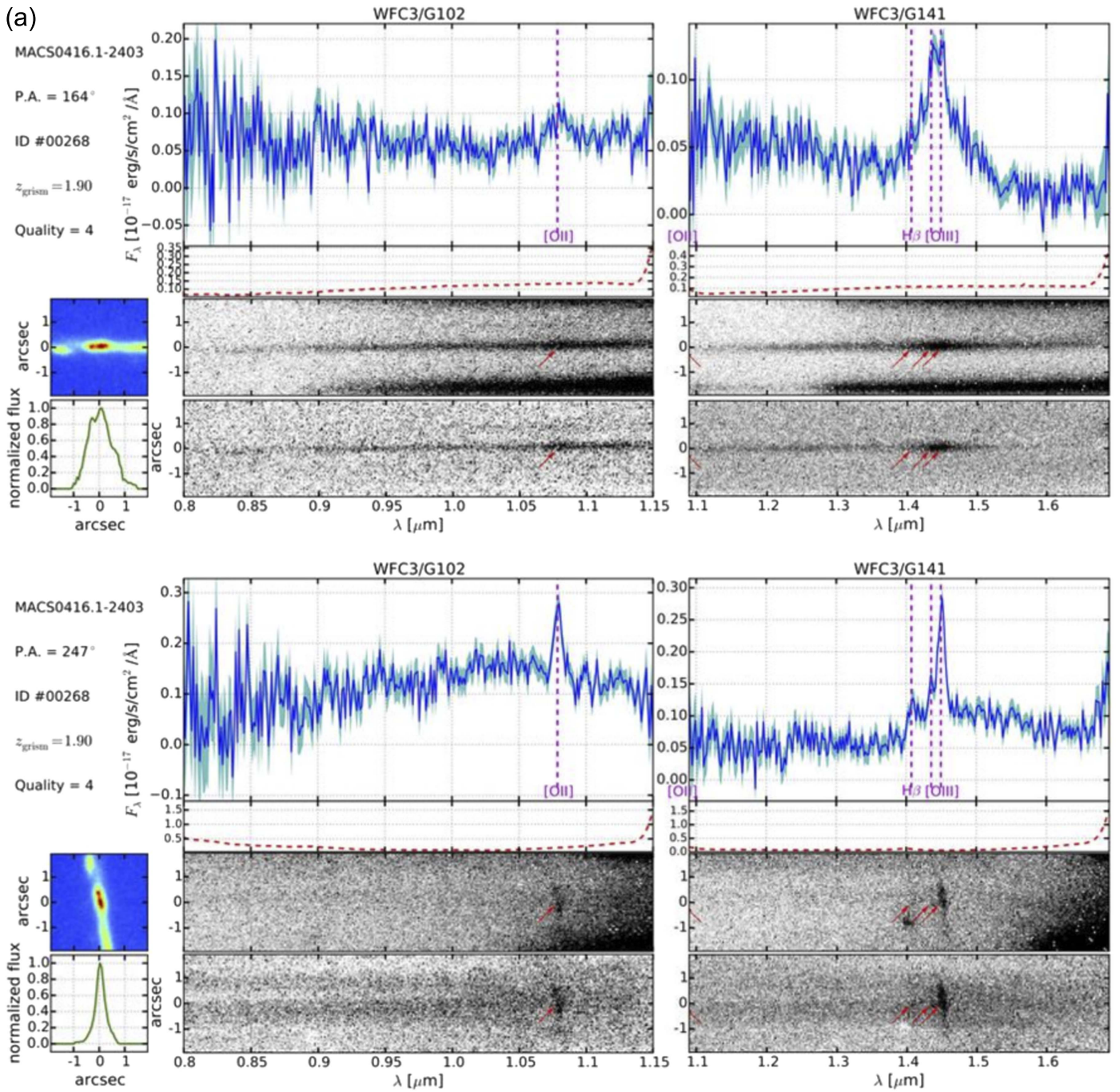

Figure 12. (a) Grism spectroscopic confirmation at $z = 1.90$ for ID #268 (arc 2.1). The two subfigures correspond to two observed P.A.s. In each subfigure, the two panels on top show the one-dimensional spectra, where the observed flux and contamination model are denoted by blue solid and red dashed lines respectively. The cyan shaded region represents the noise level. The six panels at the bottom show the two-dimensional postage stamp created from the coadded HFF+CLASH +GLASS image, the one-dimensional collapsed image, and the interlaced two-dimensional spectra without (top) and with (bottom) the contamination subtracted. In the one- and two-dimensional spectra, the identified emission lines are denoted by vertical dashed lines in magenta and arrows in red respectively. (b) Grism spectroscopic confirmation at $z = 1.89$ for object ID #248 (arc 2.2) observed at the two P.A.s shown in the two subfigures (top and bottom). Other figure details are the same as described above for object ID #268. The same emission lines observed in the spectra of arc 2.1 are observed at approximately the same wavelengths in both P.A.s of arc 2.2, showing that the two are multiple images of the same galaxy. (c) Grism spectroscopic confirmation at $z = 1.90$ for object ID #572 (arc 2.3) observed at the two P.A.s shown in the two subfigures (top and bottom). Other figure details are the same as described above for object ID #268. The same emission lines observed in the spectra of arc 2.1 and 2.2 are observed at approximately the same wavelengths in both P.A.s of arc 2.3, showing that all three are multiple images of the same galaxy. The grism redshifts are in agreement with a previous spectroscopic redshift of this system obtained by Jauzac et al. (2014) from optical spectroscopy. The complete figure set (26 elements) is available online.

(The complete figure set (26 images) is available.)

4. We obtained a map of stellar surface mass density from deep *Spitzer*/IRAC imaging data, using cluster members selected by Grillo et al. (2015). We compare this map to the total surface mass density produced from our lens model, producing a map of the projected stellar mass ratio, $f_\star$. There is significant variation in $f_\star$ throughout the cluster. $f_\star$

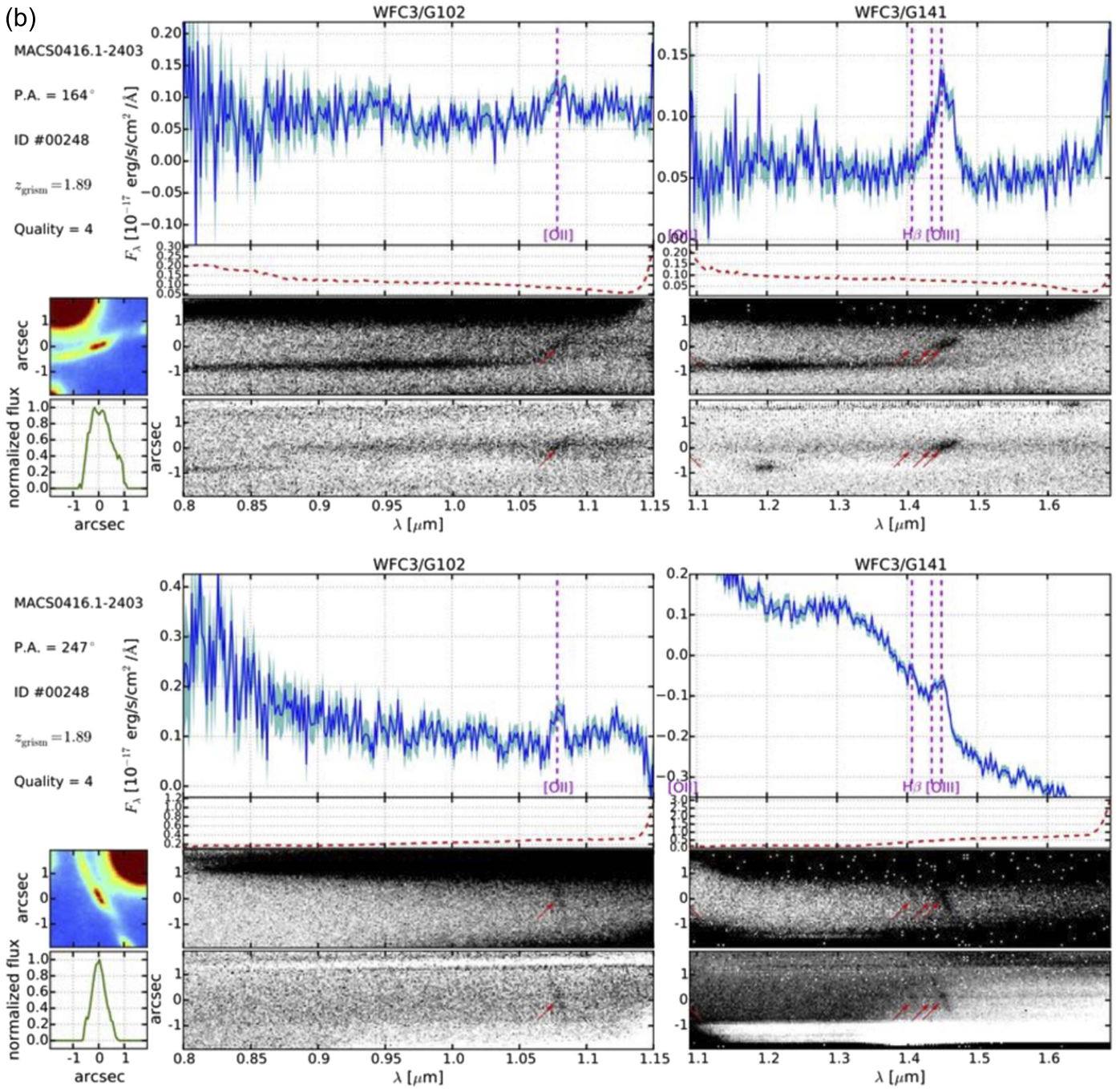

Figure 12. (Continued.)

increases with stellar surface mass density up to a stellar surface mass density of $\sim 2 \times 10^{10}\, M_\odot\, \mathrm{kpc}^{-2}$, above which our results are inconclusive. The global mean projected stellar mass fraction is $\langle f_\star \rangle = 0.009 \pm 0.003$ (stat.; 68% confidence) using a diet-Salpeter IMF. We compare our results with recent measurements of $\langle f_\star \rangle$ in the literature taken over a wide range of total cluster masses and redshifts. After correcting for different IMFs and filters used to convert stellar light to mass, we find that our measured value of $\langle f_\star \rangle$ is broadly consistent with the literature values. The one exception is with our comparison with the result from Jauzac et al. (2015a), who also measured $\langle f_\star \rangle$ for MACS 0416. However, the discrepancy can be almost entirely accounted for by the differences in the total mass maps derived from lensing.

A.H. acknowledges support by NASA Headquarters under the NASA Earth and Space Science Fellowship Program—Grant ASTRO14F-0007. This work utilizes gravitational lensing models produced by PIs Bradač, Natarajan, & Kneib (CATS), Merten & Zitrin, Sharon, and Williams, and the GLAFIC and Diego groups. The lens models were obtained from the Mikulski Archive for Space Telescopes (MAST). This work is based in part on observations made with the NASA/ESA *Hubble Space Telescope*, obtained at STScI. The data were obtained from MAST. We acknowledge support through

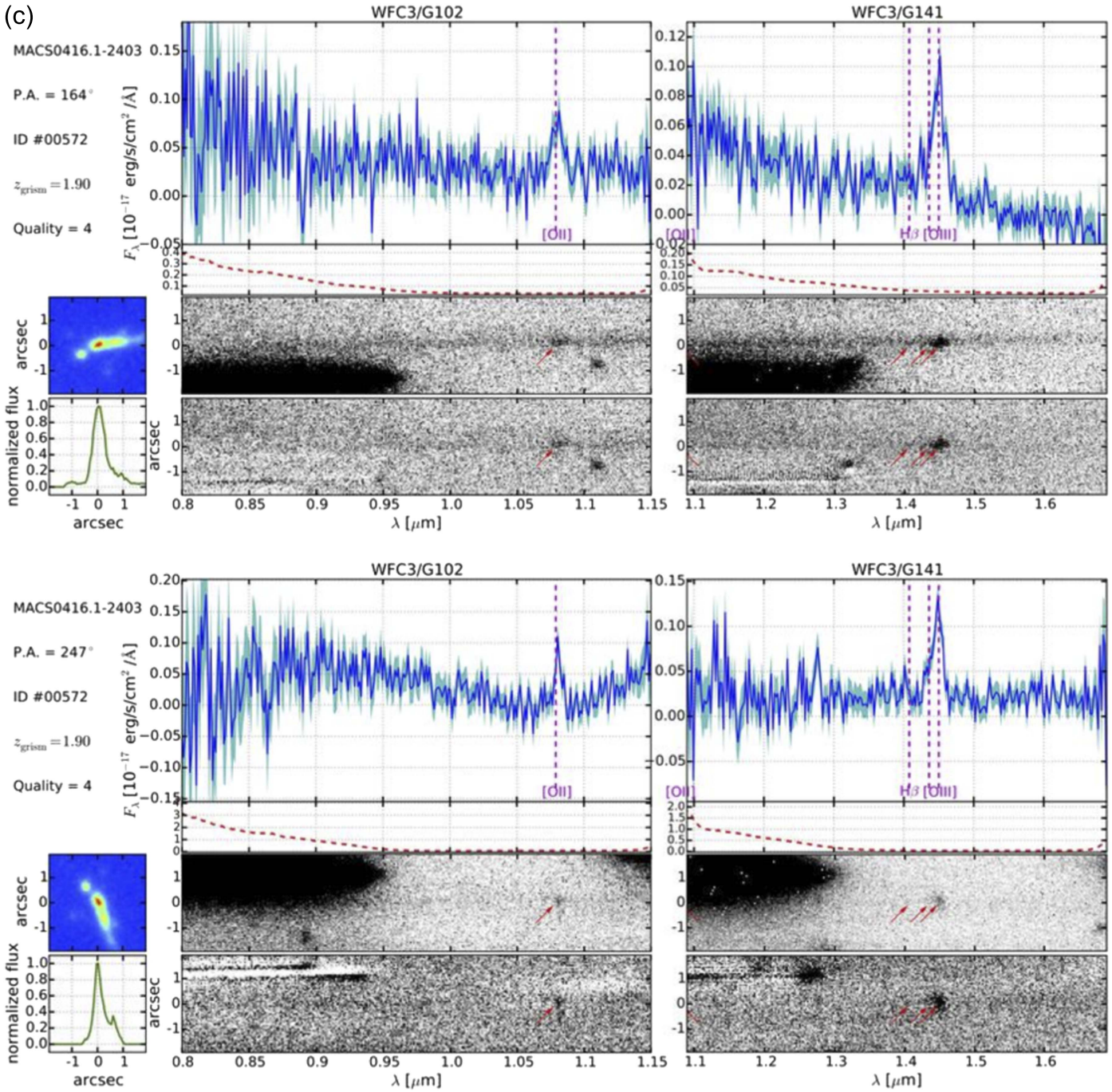

Figure 12. (Continued.)

grants HST-13459, HST-GO13177, HST-AR13235. M.B., K. H., and A.H. acknowledge support for this work through a *Spitzer* award issued by JPL/Caltech. M.B. and A.H. also acknowledge support from the special funding as part of the *HST* Frontier Fields program conducted by STScI. STScI is operated by AURA, Inc. under NASA contract NAS 5-26555. T.T. acknowledges support by the Packard Foundation through a Packard Research Fellowship, and thanks the Osservatorio Astronomico di Monteporzio Catone and the American Academy in Rome for their kind hospitality during the writing of this manuscript. B.V. acknowledges the support from the World Premier International Research Center Initiative (WPI), MEXT, Japan and the Kakenhi Grant-in-Aid for Young Scientists (B)(26870140) from the Japan Society for the Promotion of Science (JSPS).

APPENDIX A
REDSHIFT PDFS FOR THE MULTIPLY IMAGED SYSTEMS IN THE SILVER SAMPLE NOT USED IN THE LENS MODEL

In Figure 11 we show the PDFs of the individual and, where available, combined redshifts of the multiply imaged systems in the Silver sample. We believe these systems are real, but we were unable to constrain their redshifts sufficiently to include them in the lens model.

APPENDIX B
GLASS SPECTRA OF MULTIPLY IMAGED GALAXIES

In Figure 12 we show GLASS spectra confirming the redshifts of multiply imaged galaxies in MACS J0416. The uncertainty on the grism redshifts is 0.01 unless otherwise stated. The complete set of figures confirming the spectroscopic redshifts of multiple images in MACS J0416 is available as an online figure set.

REFERENCES

Annunziatella, M., Biviano, A., Mercurio, A., et al. 2014, A&A, 571, A80
Bahcall, N. A., & Kulier, A. 2014, MNRAS, 439, 2505
Balestra, I., Mercurio, A., Sartoris, B., et al. 2016, ApJS, 224, 33
Bell, E. F., McIntosh, D. H., Katz, N., & Weinberg, M. D. 2003, ApJS, 149, 289
Benítez, N. 2000, ApJ, 536, 571
Bertin, E., & Arnouts, S. 1996, A&AS, 117, 393
Bradač, M., Clowe, D., Gonzalez, A. H., et al. 2006, ApJ, 652, 937
Bradač, M., Erben, T., Schneider, P., et al. 2005, A&A, 437, 49
Bradač, M., Treu, T., Applegate, D., et al. 2009, ApJ, 706, 1201
Brammer, G. B., Pirzkal, N., McCullough, P. R., & MacKenty, J. W. 2014, Time-varying Excess Earth-glow Backgrounds in the WFC3/IR Channel, Instrument Sci. Rep. ACS (New York: STScI) (http://adsabs.harvard.edu/abs/2014wfc..rept....3B)
Brammer, G. B., Ryan, R., & Pirzkal, N. 2015, Source-dependent Master Sky Images for the WFC3/IR Grisms, Instrument Sci. Rep. ACS (New York: STScI) (http://adsabs.harvard.edu/abs/2015wfc..rept...17B)
Brammer, G. B., van Dokkum, P. G., Franx, M., et al. 2012, ApJS, 200, 13
Bruzual, G., & Charlot, S. 2003, MNRAS, 344, 1000
Burke, C., Hilton, M., & Collins, C. 2015, MNRAS, 449, 2353
Caminha, G. B., Grillo, C., Rosati, P., et al. 2016, arXiv:1607.03462
Castellano, M., Amorín, R., Merlin, E., et al. 2016, A&A, 590, A31
Christensen, L., Richard, J., Hjorth, J., et al. 2012, MNRAS, 427, 1953
Clowe, D., Bradač, M., Gonzalez, A. H., et al. 2006, ApJL, 648, L109
Coe, D., Benítez, N., Sánchez, S. F., et al. 2006, AJ, 132, 926
Coe, D., Zitrin, A., Carrasco, M., et al. 2013, ApJ, 762, 32
Dahlen, T., Mobasher, B., Faber, S. M., et al. 2013, ApJ, 775, 93
Diego, J. M., Broadhurst, T., Molnar, S. M., Lam, D., & Lim, J. 2015a, MNRAS, 447, 3130
Diego, J. M., Broadhurst, T., Zitrin, A., et al. 2015b, MNRAS, 451, 3920
Ebeling, H., Edge, A. C., & Henry, J. P. 2001, ApJ, 553, 668
Erben, T., Van Waerbeke, L., Bertin, E., Mellier, Y., & Schneider, P. 2001, A&A, 366, 717
Fazio, G. G., Hora, J. L., Allen, L. E., et al. 2004, ApJS, 154, 10
Fioc, M., & Rocca-Volmerange, B. 1997, A&A, 326, 950
Gonzaga, S. 2012, The DrizzlePac Handbook (New York: STScI)
Gonzalez, A. H., Sivanandam, S., Zabludoff, A. I., & Zaritsky, D. 2013, ApJ, 778, 14
Grillo, C., Suyu, S. H., Rosati, P., et al. 2015, ApJ, 800, 38
Hoekstra, H., Franx, M., Kuijken, K., & Squires, G. 1998, ApJ, 504, 636
Jauzac, M., Clément, B., Limousin, M., et al. 2014, MNRAS, 443, 1549
Jauzac, M., Jullo, E., Eckert, D., et al. 2015a, MNRAS, 446, 4132
Jauzac, M., Richard, J., Jullo, E., et al. 2015b, MNRAS, 452, 1437
Johnson, T. L., Sharon, K., Bayliss, M. B., et al. 2014, ApJ, 797, 48
Kaiser, N., Squires, G., & Broadhurst, T. 1995, ApJ, 449, 460
Koester, B. P., McKay, T. A., Annis, J., et al. 2007, ApJ, 660, 239
Livermore, R. C., Finkelstein, S. L., & Lotz, J. M. 2016, arXiv:1604.06799
Lotz, J. M., Koekemoer, A., Coe, D., et al. 2016, arXiv:1605.06567
Luppino, G. A., & Kaiser, N. 1997, ApJ, 475, 20
Mann, A. W., & Ebeling, H. 2012, MNRAS, 420, 2120
Massey, R., Schrabback, T., Cordes, O., et al. 2014, MNRAS, 439, 887
Meneghetti, M., Natarajan, P., Coe, D., et al. 2016, arXiv:1606.04548
Merlin, E., Amorín, R., Castellano, M., et al. 2016, A&A, 590, A30
Merten, J., Meneghetti, M., Postman, M., et al. 2015, ApJ, 806, 4
Momcheva, I. G., Brammer, G. B., van Dokkum, P. G., et al. 2015, ApJS, 225, 27
Newman, A. B., Treu, T., Ellis, R. S., & Sand, D. J. 2013, ApJ, 765, 25
Ogrean, G. A., van Weeren, R. J., Jones, C., et al. 2015, ApJ, 812, 153
Oke, J. B. 1974, ApJS, 27, 21
Planck Collaboration 2015, A&A, 594, A13
Postman, M., Coe, D., Benítez, N., et al. 2012, ApJS, 199, 25
Press, W. H. 1997, in Unsolved Problems in Astrophysics, ed. J. N. Bahcall & J. P. Ostriker (Princeton, NJ: Princeton Univ. Press)
Richard, J., Jauzac, M., Limousin, M., et al. 2014, MNRAS, 444, 268
Rodney, S. A., Patel, B., Scolnic, D., et al. 2015a, ApJ, 811, 70
Rodney, S. A., Strolger, L.-G., Kelly, P. L., et al. 2015b, ApJ, 820, 50
Salpeter, E. E. 1955, ApJ, 121, 161
Sand, D. J., Treu, T., Ellis, R. S., Smith, G. P., & Kneib, J. 2008, ApJ, 674, 711
Schmidt, K. B., Treu, T., Bradač, M., et al. 2016, ApJ, 818, 38
Schmidt, K. B., Treu, T., Brammer, G. B., et al. 2014, ApJL, 782, L36
Schrabback, T., Erben, T., Simon, P., et al. 2007, A&A, 468, 823
Schrabback, T., Hartlap, J., Joachimi, B., et al. 2010, A&A, 516, A63
Sharon, K., Gladders, M. D., Rigby, J. R., et al. 2014, ApJ, 795, 50
Treu, T., Brammer, G., Diego, J. M., et al. 2016, ApJ, 817, 60
Treu, T., & Ellis, R. S. 2014, arXiv:1412.6916
Treu, T., Schmidt, K. B., Brammer, G. B., et al. 2015, ApJ, 812, 114
Umetsu, K., Medezinski, E., Nonino, M., et al. 2014, ApJ, 795, 163
Vulcani, B., Poggianti, B. M., Aragón-Salamanca, A., et al. 2011, MNRAS, 412, 246
Wang, X., Hoag, A., Huang, K.-H., et al. 2015, ApJ, 811, 29
Werner, M. W., Roellig, T. L., Low, F. J., et al. 2004, ApJS, 154, 1
York, D. G., Adelman, J., Anderson, J. E., Jr., et al. 2000, AJ, 120, 1579
Zheng, W., Postman, M., Zitrin, A., et al. 2012, Natur, 489, 406
Zitrin, A., Fabris, A., Merten, J., et al. 2015, ApJ, 801, 44
Zitrin, A., Meneghetti, M., Umetsu, K., et al. 2013, ApJL, 762, L30
Zitrin, A., Zheng, W., Broadhurst, T., et al. 2014, ApJL, 793, L12